pubs.acs.org/Biomac

Article

Protein-Specific Crowding Accelerates Aging in Protein Condensates

Mateusz Brzezinski, Pablo G. Argudo, Tom Scheidt, Miao Yu, Elnaz Hosseini, Anke Kaltbeitzel, Edward A. Lemke, Jasper J. Michels,* and Sapun H. Parekh*

Cite This: *Biomacromolecules* 2025, 26, 2060−2075

Read Online

ACCESS | Metrics & More | Article Recommendations | Supporting Information

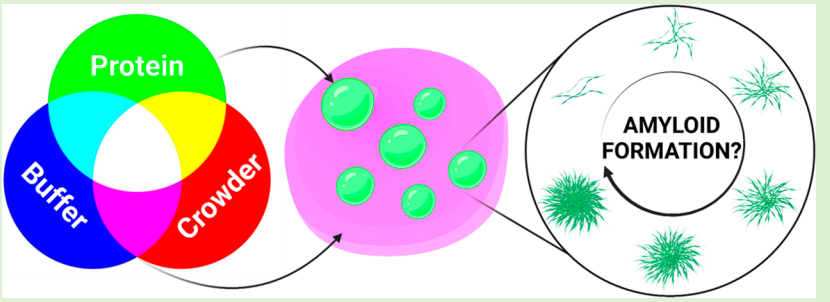

ABSTRACT: Macromolecular crowding agents, such as poly(ethylene glycol) (PEG), are often used to mimic cellular cytoplasm in protein assembly studies. Despite the perception that crowding agents have an inert nature, we demonstrate and quantitatively explore the diverse effects of PEG on the phase separation and maturation of protein condensates. We use two model proteins, the FG domain of Nup98 and bovine serum albumin (BSA), which represent an intrinsically disordered protein and a protein with a well-established secondary structure, respectively. PEG expedites the maturation of Nup98, enhancing denser protein packing and fortifying interactions, which hasten beta-sheet formation and subsequent droplet gelation. In contrast to BSA, PEG enhances droplet stability and limits the available solvent for protein solubilization, inducing only minimal changes in the secondary structure, pointing toward a significantly different role of the crowding agent. Strikingly, we detect almost no presence of PEG in Nup droplets, whereas PEG is moderately detectable within BSA droplets. Our findings demonstrate a nuanced interplay between crowding agents and proteins; PEG can accelerate protein maturation in liquid−liquid phase separation systems, but its partitioning and effect on protein structure in droplets is protein specific. This suggests that crowding phenomena are specific to each protein-crowding agent pair.

INTRODUCTION

The study of proteins and their interactions is a cornerstone of modern biochemistry and molecular biology. One emerging phenomenon in this field is phase separation (PS), which appears to underlie, at least in part, the formation of membraneless organelles (MLOs) inside cells.[1,2] This process in protein-based systems can be driven by multivalent protein−protein interactions, leading to the formation of droplet-like structures that compartmentalize biomolecules without the need for a surrounding lipid barrier. Crucially, these protein interactions and the ensuing PS can be heavily influenced by the crowded nature of the cellular environment.[3] In this context, the role of crowding agents, which mimic the dense intracellular milieu, is being increasingly recognized and investigated.[4] Crowding agents affect PS through several key mechanisms.[5] One mechanism is volume exclusion, a fundamental principle underpinning their function. Volume exclusion promotes PS by reducing the available volume for other macromolecules, thereby inducing segregation and formation of distinct phases.[6,7] Additionally, crowding agents typically retard diffusion rates of proteins.[8] Lastly, by inducing a dehydration effect, crowding agents strip away water molecules that may otherwise be associated with biomolecules, making protein−protein interactions more favorable and further promoting PS.[9] Molecular partitioning of crowding agents follows one of two pathways: competitive (segregative) and cooperative (associative).[10−12] In segregative PS, protein and crowding agent macromolecules partition into distinct phases to minimize interactions. In contrast, in associative PS, both protein and crowding agent macromolecules coalesce into a single phase, driven by mutual affinity.

Polyethylene glycol (PEG) is a widely used crowding agent in biochemical studies to mimic the intracellular environment. It is a variable-molecular-weight polymer composed of repeating ethylene oxide units. PEG is hydrophilic and highly soluble in

Received: May 7, 2024
Revised: November 19, 2024
Accepted: November 21, 2024
Published: December 9, 2024

https://doi.org/10.1021/acs.biomac.4c00609
Biomacromolecules 2025, 26, 2060−2075

aqueous buffers, in particular at low molecular weight.[13−15] It typically does not form specific binding interactions but can interact nonspecifically with proteins or other biomolecules.[16−19] For this reason, it has been perceived as an "inert" crowding agent.[20,21] One notable exception is its apparent ability to bind to lysine residues via a crown-ether type motif.[22] In any case, it will at least interact with its environment in a nonspecific way. Owing to these properties, PEG has been used to effectively mimic the crowded nature of a typical cell interior without introducing unnecessary complications from specific noncovalent interactions.[4] Recent research indicates a shift in our understanding of PEG's role in PS. Contrary to its traditional classification as an "inert" crowding agent, newer studies suggest that PEG can colocalize within protein condensates and actively participate in an associative PS.[12,23] This highlights PEG's potential contribution to the formation and characteristics of the resulting phase-separated structures.

Nucleoporins (Nups), key components of the nuclear pore complex (NPC), belong to the family of intrinsically disordered proteins (IDPs) that lack a well-defined structure in their native state, providing them with exceptional conformational and structural flexibility.[24] Within the highly crowded environment of the NPC, these Nups play an indispensable role in controlling molecular traffic between the nucleus and the cytoplasm.[25] Under certain conditions, Nups can undergo further transitions, leading to fibrillation, where they self-assemble into fiber-like structures in vitro.[26,27] This transition is thought to be propelled by hydrophobic interactions between phenylalanine/glycine (FG) repeat motifs, suggesting a key role for nonpolar forces in driving the transition toward fibrillation. The potential sequence of transitions—liquid to gel to fibrils—showcases the adaptability of Nups and their intricate contribution to cellular function.[28] However, this uncontrolled aggregation and subsequent deposition of other IDP families such as FUS (FUsed in Sarcoma) or TAU (Tubulin Associated Unit) can disrupt normal cellular functions and is associated with a range of neurodegenerative disorders, including Alzheimer's, Parkinson's, and Huntington's diseases.[29−33] The self-assembly of these proteins is often driven by beta (β)-sheet formation, which allows stable aggregates to form via an increase in intermolecular hydrogen bonding facilitated by the exposure of hydrophobic regions.[34,35] Consequently, understanding the influence of the nucleoporin environment on such a structural transition of Nups is of paramount importance. This knowledge will provide critical insights into the mechanistic pathways of protein aggregation and its role in disease.[36] Many studies have explored the impact of PEG and other crowding agents on different proteins, spanning both IDPs and those with well-defined secondary structures.[37,38] However, our understanding regarding the influence of crowding on the kinetics of the structural maturation in PS-formed protein condensates remains incomplete and warrants further investigation.[39,40]

In the present investigation, we delve into the intricacies of the kinetic aspect of protein condensate maturation, focusing specifically on the structural transformation of initially liquid-like protein condensates in the presence and absence of a PEG crowding agent. We furthermore analyze, discuss, and categorize the phase behavior of the protein/PEG/buffer mixtures. Where possible, we map out and model the phase diagram by quantifying the composition of the condensates as well as the coexisting dilute phase. We implement broadband coherent anti-Stokes Raman scattering (BCARS) and fluorescence recovery after photobleaching (FRAP) to examine the "aging" states of Nup98 under varying crowding conditions and time frames. Additionally, we include a comparison with PS of a solution of bovine serum albumin (BSA), a well-studied protein with defined folding. Through this study, we aim to shed light on the specifics of how molecular crowding influences protein condensate formation and transformation or maturation and whether this influence translates universally across both disordered and folded protein assemblies or remains specific to a certain class of proteins.

MATERIALS AND METHODS

Nup Purification, Solutions, and Labeling. The FG domain of *Homo sapiens* Nup98 (spanning 1−505 amino acids, excluding the Gle2-binding domain (GLEBS; 157−213 amino acids), a structured domain interspersed between the two FG domains) was expressed in *Escherichia coli* BL21 AI cells. Detailed protocols for the expression and purification are available in the Methods Section of our previous publication.[84] The purified Nup98 was concentrated to a final concentration of 165 μM using 3 kDa molecular weight cut-off (MWCO) centrifugal filters (Merck Millipore) in a solution of 2 M guanidine hydrochloride (GdmCl), 0.2 mM tris(2-carboxyethyl)-phosphine (TCEP), and 50 mM Tris−HCl, pH 8, with the concentration measured by the Pierce BCA Protein Assay Kit (23,227, Thermo Fisher). The proteins were flash-frozen and stored at −80 °C.

Full NUP98 FG domain sequence without the GLEBS domain is as follows: MFNKSFGTPFGGGTGGFGTTSTFGQNTGFGTTS-GGAFGTSAFGSSNNTGGLFGNSQTKPGGLFGTSSFSQPAT-STSTGFGFGTSTGTANTLFGTASTGTSLFSSQNNAFAQN-KPTGFGNFGTSTSSGGLFGTTNTTSNPFGSTSGSLFGPSSFTA-AGPQNQVGAGTTTGLFGSSPATSSATGLFSSSTTNSGFA-YGQNKTAFGTSTTGFGTNPGGLFGQQNQQTTSLFSKPFGQ-ATTTQNTGFSFGNTSTIGQPSTNTMGLFGVTQASQPG-GLFGTATNTSTGTAFGTGTGLFGQTNTGFGAVGSTLFG-NNKLTTFGSSTTSAPSFGTTSGGLFGFGTNTSGNSIFG-SKPAPGTLGTGLGAGFGTALGAGQASLFGNNQPKIGGP-LGTGAFGAPGFNTTTATLGFGAPQAPVALTDPNASAAQQ-AVLQQHINSLTYSPFGDSPLFRNP.

The molecular weight of this NUP98 FG domain (1−448) is 43.56 kDa. For labeling, the purified Nup98 FG domain, with a single cysteine mutation (A221C), was exchanged into 4 M GdmCl, 1× PBS, 0.1 mM EDTA, and 0.2 mM TCEP, pH 7. Labeling with Alexa Fluor 488 maleimide (A10254, Thermo Fisher) was performed at a molar ratio of 1:2 (dye/protein) overnight at 4 °C. The reaction was quenched with 10 mM DTT in 4 M GdmCl and 1× PBS, pH 7. Unreacted dye was washed off by using a 3 kDa MWCO centrifugal filter, and the labeled protein was further purified with Superdex 200. Pure fractions were selected, pooled, and concentrated, and the final concentration was measured using a Duetta absorbance spectrometer (Horiba). Protein was flash-frozen and stored at −80 °C. For all fluorescence-based investigations, the Nup98 solution was doped with 1% of a fluorescently labeled version of Nup98.

BSA Solutions and Labeling. BSA Fraction V (1126GR050, neoFroxx) was dissolved in 10× PBS buffer overnight at a constant temperature of 25 °C using a Thermoblock to ensure complete dissolution. The solution was then transferred to a syringe fitted with a 0.22 μm polyvinylidene difluoride (PVDF) filter and subsequently filtered to remove any potential contaminants. The purified aliquots were flash-frozen and stored at −80 °C until further use. The final concentration of the solution was confirmed to be 125 μM (8.25 mg/mL) using the Pierce BCA Protein Assay Kit (23,227, Thermo Fisher).

The BSA sequence used in our study is as follows: MKWVTF-ISLLLLFSSAYSRGVFRRDTHKSEIAHRFKDLGEEHFKGLV-LIAFSQYLQQCPFDEHVKLVNELTEFAKTCVADESHA-GCEKSLHTLFGDELCKVASLRETYGDMADCCEKQE-PERNECFLSHKDDSPDLPKLKPDPNTLCDEFKADEKK-FWGKYLYEIARRHPYFYAPELLYYANKYNGVFQECCQA-EDKGACLLPKIETMREKVLASSARQRLRCASIQKFGE-RALKAWSVARLSQKFPKAEFVEVTKLVTDLTKVHKECCHGD-

https://doi.org/10.1021/acs.biomac.4c00609
Biomacromolecules 2025, 26, 2060−2075

LLECADDRADLAKYICDNQDTISSKLKECCDKPLLEKSHCIA-EVEKDAIPENLPPLTADFAEDKDVCKNYQEAKDAFLGSFL-YEYSRRHPEYAVSVLLRLAKEYEATLEECCAKDDPH-ACYSTVFDKLKHLVDEPQNLIKQNCDQFEKLGEYGFQ-NALIVRYTRKVPQVSTPTLVEVSRSLGKVGTRCCTKPESERMP-CTEDYLSLILNRLCVLHEKTPVSEKVTKCCTESLVNRRPCFS-ALTPDETYVPKAFDEKLFTFHADICTLPDTEKQIKKQT-ALVELLKHKPKATEEQLKTVMENFVAFVDKCCAADDKEACFA-VEGPKLVVSTQTALA. The molecular weight of BSA (25−607) is 66.43 kDa.

For fluorescent BSA, fluorescein-labeled BSA (BSA-FITC), albumin-fluorescein isothiocyanate conjugate (A9771, Merck) was used. The lyophilized conjugate was reconstituted in 10× PBS to a concentration of 500 μM (33 mg/mL), following the procedure previously outlined. Subsequent to preparation, the protein solution was flash-frozen and stored at −80 °C until required. For all fluorescence-driven experiments, the standard BSA solution was enriched with 1% fluorescently labeled BSA.

PEG Solutions. Polyethylene glycol (PEG) with a molecular weight of 4000 g/mol (95,904, Merck) was dissolved in either 1× transport buffer (TB) (TB; 20 mM HEPES, 110 mM KOAc, 5 mM NaOAc, 2 mM $Mg(OAc)_2$, 1 mM EGTA, and 2 mM DTT, pH 7.3)[85] (Nup98 studies) or 1× PBS (BSA studies). This was achieved through overnight incubation at 40 °C with continuous stirring on a hot plate, resulting in a final concentration of 40% (w/v). This stock solution was then systematically diluted to generate a series of working concentrations suitable for our studies: 0%, 2.5%, 5%, 10%, and 30% for investigations on Nup98 and 10%, 20%, and 30% for BSA studies. All solutions were stored at −80 °C.

Condensate Sample Preparation and Preservation. For our time-dependent experiments for each sample, a 24 × 60 mm, #1, nonmodified glass coverslip was prepared with two parallel strips of double-sided tape, leaving an approximate gap of 15 mm. Subsequently, 2 μL of the protein solution was carefully pipetted into the gap, followed by the addition of 20 μL of the buffer with PEG. After allowing about a minute for the sample to stabilize, a 20 × 20 mm, #1 glass coverslip was positioned over the sample to create a seal. The top coverslip was then firmly pressed onto the double-sided tape, ensuring a secure adhesion. To further enhance the seal and maintain an airtight environment, each of the four edges of the top coverslip was sealed using a quick-drying, cyanoacrylate-based adhesive (UHU, super glue). This comprehensive preparation ensured an optimal environment for our subsequent time-dependent microscopy studies, minimizing potential evaporation or contamination. Impressively, this robust setup displayed no leakage even after 1 month of storage, thereby reinforcing the stability and reliability of our experimental conditions.

Fluorescence Recovery after Photobleaching. FRAP experiments were conducted using a Leica SP8 confocal microscope with a 63 × 1.20 NA water immersion objective. We utilized a 488 nm laser line for studies involving Nup98 and both 488 and 496 nm laser lines for BSA experiments. All image stacks acquired maintained a consistent resolution of 512 × 512 pixels. The scanner was configured to a scanning frequency of 700 Hz, allowing for a cycle time of 0.743 s. A total of 165 frames were recorded for each sample: the first 5 frames were captured as "pre-bleach" images using a laser power of 5%, followed by 10 bleach frames with the laser power locally intensified to 100%, and finally 150 postbleach frames with a laser power of 5%. Throughout the imaging process, the pinhole size was held constant at 100 nm to ensure consistency in the collected data. Zoom was also maintained within a range of 15−30×. This imaging setup allowed for high-resolution and consistent data collection across all FRAP experiments. Subsequent to data acquisition, a custom Python script was employed to process the collected data. This script was designed to facilitate the simultaneous analysis of four bleached regions of interest (ROIs) while accounting for an additional background ROI (consisting of an empty plane) and a reference ROI (comprising the entire sample plane). Following this preliminary processing, data were exported to easyFRAP, an online FRAP analysis tool.[86−88]

Broadband Coherent Anti-Stokes Raman Scattering Microscopy. Raman measurements were performed using a home-built broadband coherent anti-Stokes Raman scattering (BCARS) microscope, the detailed configuration of which has been documented in prior work.[89] In essence, the pump/probe and Stokes pulses are created in a dual-output, subnanosecond laser source (CARS-SM-30, Leukos). These pulses are then synchronously overlapped in space and time at the sample plane of an inverted microscope (Eclipse Ti−U, Nikon) and tightly focused onto the sample using a 0.85 NA air objective (LCPlan N, Olympus). The BCARS signal, once isolated from the excitation pulses, is focused onto the slit of a spectrograph (Shamrock 303i, Andor). This disperses the spectral components onto a cooled CCD camera (Newport DU920P-BR-DD, Andor). Samples are positioned with the coverslip facing the collector and scanned using a piezo stage (Nano-PDQ 375 HS, Mad City Laboratories) controlled by LabView 2015 (National Instruments) software. Following data collection, the amassed hyperspectral data undergo processing in IgorPro (WaveMetrics). The Raman-like spectra are retrieved through a modified Kramers−Kronig transform.[90] All spectra presented in this paper were phase-retrieved using buffer alone, with no macromolecules as a reference spectrum, and any background phase is removed using a Savitzky−Golay filter with a second order polynomial and a window size of approximately 400 cm^{-1}. This protocol allowed us to acquire and interpret high-quality spectral data from our samples.

For the deconvolution of the Nup98 amide I band, we utilized a custom Python script. This script facilitated the generation of an initial seed for the parameters of the Lorentzian peaks. We derived these initial estimates in accordance with our prior published work.[91] Upon establishing these initial parameters, we input them into the peak analyzer function of OriginLab Pro. This software further refined the deconvolution and produced the final resolution of the peaks.

To analyze BSA/PEG concentrations via CH stretch peak fitting, we employed a custom Python script based on the BCARS spectra of 4 mM BSA and 75 mM PEG reference samples for the CH region (2800−3100 cm^{-1}). These samples were processed and measured following the same protocols as those described above. Spectral fitting of phase-retrieved spectra was conducted in the range of 2820−3050 cm^{-1}, with each spectrum normalized to the highest peak of the sample. BSA and PEG concentrations were determined by fitting the normalized spectrum to a weighted sum of the pure BSA and PEG spectra, with each component being weighted by a coefficient to best fit the experimental spectrum. The fitting coefficients were then transformed into concentrations using a reverse normalization procedure to correlate with the BSA or PEG reference concentrations. To account for variations linked to different alignments and to make spectra from day-to-day quantitatively comparable, we collected Raman-like spectra of water prior to each sample measurement. This was used for subsequent rescaling, ensuring that potential deviations were minimized and thus enabling accurate and reliable analysis.

Thioflavin T Microscopy. Thioflavin T (ThT; T3516) was purchased from Sigma. A final concentration of 40 μM ThT was diluted from a 5 mM stock in Milli-Q water, determined by absorbance at 412 nm with ε = 31,600 M^{-1} cm^{-1}. For Nup98 droplets, ThT was added to TB prior to mixing with PEG. For BSA droplets, ThT was added independently immediately after dilution of BSA with PEG solutions. Microscopy for ThT was performed using epifluorescence microscopy (Olympus IX70) with a 40× objective and standard filter set for FITC/GFP provided by the manufacturer.

RESULTS AND DISCUSSION

PEG Crowding Drives Segregative Nup98 Condensation, Accelerates Structural Maturation, and Reduces Molecular Mobility. Liquid−liquid PS of Nup98, whether in the presence or absence of PEG, results in the formation of droplet-like condensates. The size of these condensates varies with the concentration of the PEG crowding agent and the condensate population namely their location, size, and shape are nonuniform on the sample, suggesting a kinetic process at work during condensate formation (Figure S1). To obtain a comparable understanding of the chemical composition of

https://doi.org/10.1021/acs.biomac.4c00609
Biomacromolecules 2025, 26, 2060−2075

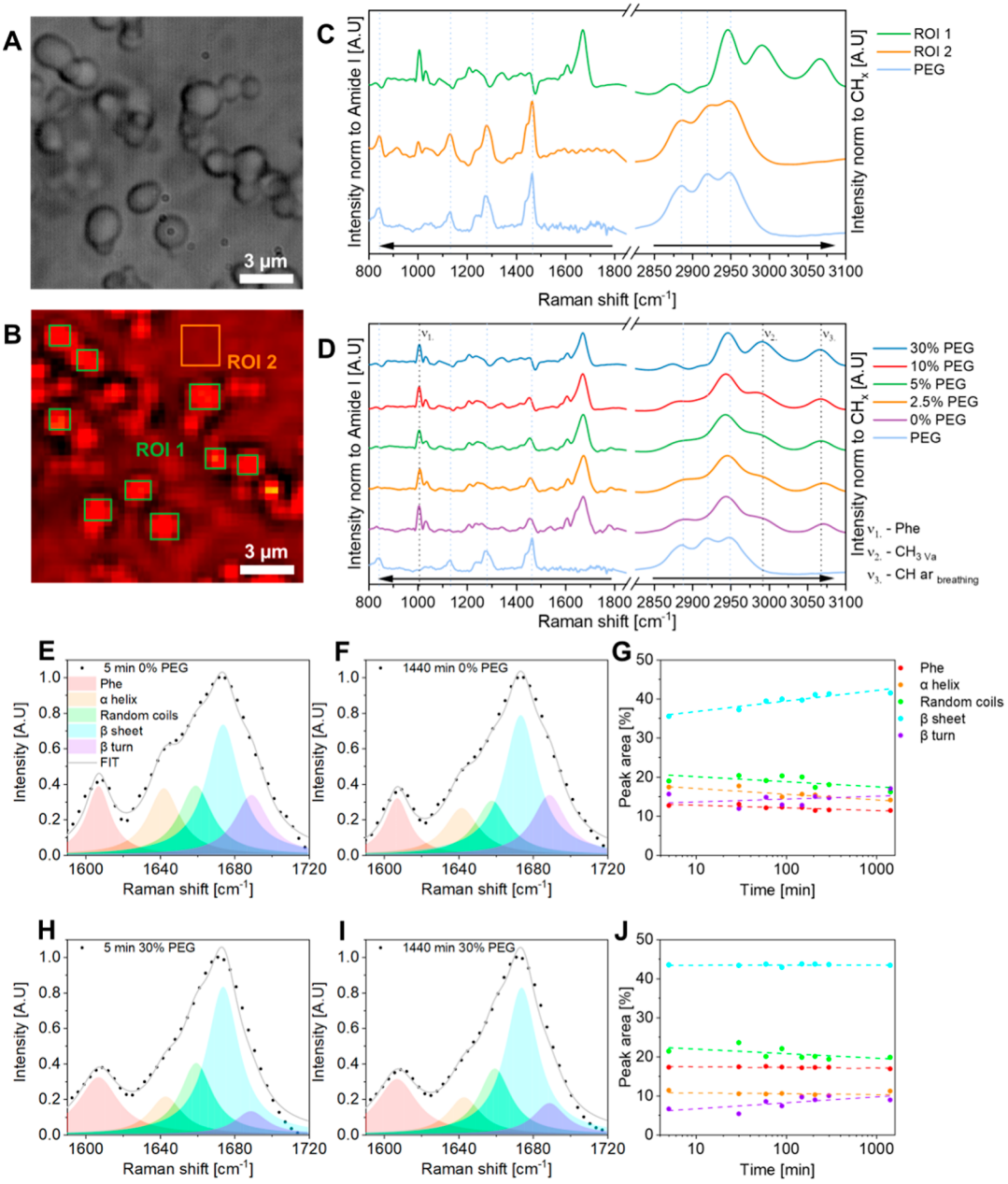

Figure 1. Molecular microscopy of Nup98:PEG condensate aging. In situ (A) BF image and (B) BCARS map imaging of the same Nup condensates formed by mixing 1:10 Nup 0.165 mM with PEG 4 kDa 75 mM (30% m/v). Both images were captured 24 h after initiation of LLPS. BCARS map shows averaged CH stretch intensity and is integrated over 2820−3020 cm^{-1} with a pixel size of 0.375 × 0.375 μm. On the BCARS map, ROI 1 marked green, represents a selected part of the droplet phase, and ROI 2 marked orange, represents a selected part of the continuous phase of a sample. (C) Normalized fingerprint and CH stretch spectra comparison of ROI 1 and ROI 2 to 75 mM PEG reference sample. (D) Normalized fingerprint and CH stretch spectra of droplet phase for different PEG concentration systems measured 5 min after initializing liquid−liquid phase separation (LLPS) and 75 mM PEG reference sample. amide I spectra deconvolution for (E) 0% PEG system at 5 min and (F) 24 h and (H) 30% PEG system at 5 min and (I) 24 h. Thick lines are fit curves which are the sum of all subpeaks, and circular points indicate the experimental data values. Every deconvolution was based on the same set of initial parameters with fixed position and fixed fwhm of all Lorentzian peaks and freedom of 5 and 4 cm^{-1}, respectively. Participation of subpeaks in amide I deconvoluted spectra over time for (G) 10% PEG and (J) 30% PEG systems. Dashed lines are linear fit and circular points represent a peak area for each time of maturation.

both the continuous and droplet phases across all PEG concentrations, we targeted regions in the samples where both phases (droplets and a continuous phase) were present (Figure 1A) (shown for 30% (w/v) PEG). Immediately obvious from the bright field imaging are overlapping droplet structures, implying the ability to form unified condensates through droplet coalescence. This indicates the liquidity of such droplets, at least during their formation, as the structure of condensates was stable during the measurement 24 h post droplet formation. BCARS imaging allowed us to acquire intensity maps spanning the spectral range from 700 to 3700 cm^{-1} and to correlate the spatial distribution of each phase with their respective CARS spectra to understand chemical distribution across sample plane (Figure 1B). For an in-depth analysis of the diversity of chemical composition inside and outside of the condensates, we made regions of interest using a representative number of pixels for

https://doi.org/10.1021/acs.biomac.4c00609
Biomacromolecules 2025, 26, 2060−2075

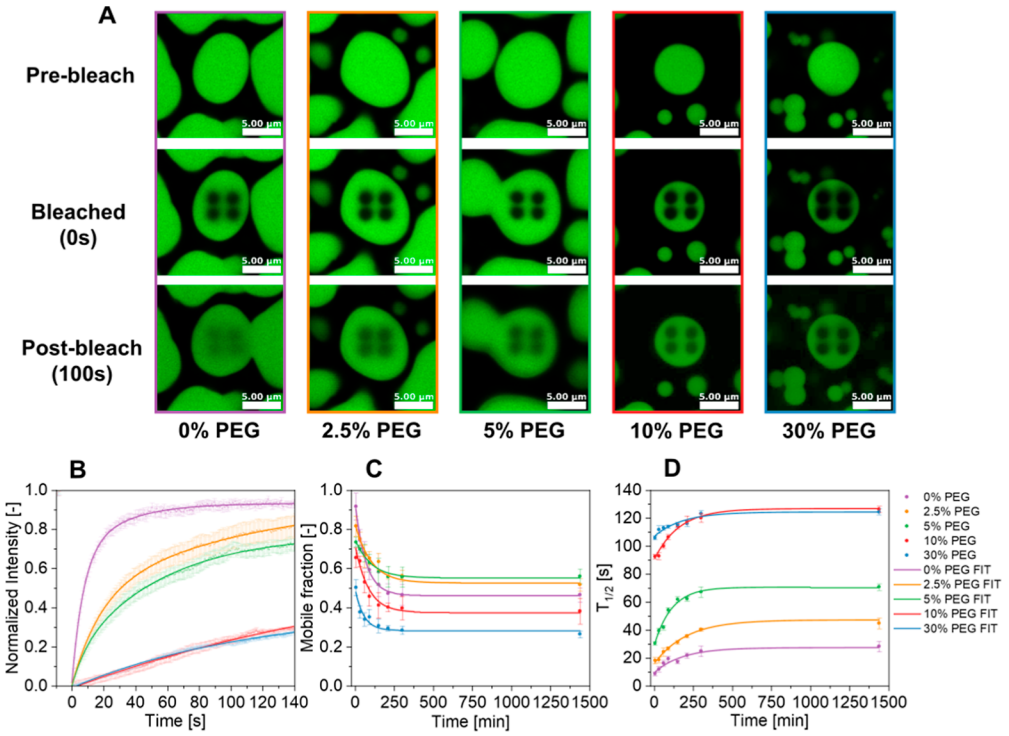

Figure 2. FRAP of Nup98:PEG condensates shows reduced recovery with maturation time. (A) Representative images from FRAP experiments of 1% Alexa Fluor 488-labeled Nup 0.165 mM condensates for 0%−30% PEG systems captured 5−30 min after initializing LLPS. Each sample was bleached simultaneously in four circular spots with the same diameter of 1.5 μm. (B) Normalized fluorescence intensity of 0%−30% PEG systems over time after bleaching. Presented curves apply to 5 min maturated samples. (C) Dependence of the mobile fraction on maturation time. (D) Dependence of the half-time fluorescence recovery on droplet age. In graphs (B−D), thick lines are fit curves, circular points indicate the average values of 4 bleached regions, and error bars show the standard deviation.

both phases based on the visual representation of the intensity map. Interestingly, these regions exhibited distinct chemical variations (Figure 1C). The droplet phase exhibited a typical protein fingerprint region profile with pronounced peaks at ∼1670 cm^{-1} for amide I and ∼1000 cm^{-1}, indicative of phenylalanine residues. Additionally, the C−H stretching profile for both CH_2 and CH_3 groups occurred in the 2920−3030 cm^{-1} region, along with a notable peak at around 3065 cm^{-1}, which comes from aromatic groups of amino acids.[41−45] In stark contrast, the continuous phase largely lacked these peaks but showed vibrations associated with PEG, if present in the mixture, or nothing when the sample was protein and buffer alone. The continuous phase with PEG and Nup98 in the sample is characterized by a triple peak in the C−H stretching vibration region of 2850−3000 cm^{-1} as well as numerous peaks in the fingerprint region correlated to C−C and C−O stretching and C−C−O bending and other chain bending modes.[46−49]

The difference in spectra from the droplet versus continuous phase regions implies that the crowding agent, PEG, is primarily situated in the continuous phase, with minimal to no presence in the droplet phase, which was supported when linear unmixing was unable to identify PEG in the droplet phase. Conversely, the continuous phase demonstrates a relative protein deficiency; the signal emanating from the continuous phase closely mirrors that from the prevalent PEG, with no discernible trace of protein. From these observations, we deduce that the Nup98:PEG/buffer mixture exhibits fully segregative PS, where the macromolecular solutes each end up in a separate coexisting phase.[11,20] Apparently, the interaction between Nup98 and PEG is effectively repulsive (both having a higher affinity with the like species compared to the unlike species), which is consistent with the notion that PEG is hydrophilic and Nup98 relatively hydrophobic due to the high density of apolar FG repeats in its primary structure. Recently, it has been shown that titration of such "depletant crowders" can be used to quantify polymer−solvent interaction.[50] Our observation seemingly contradicts previous work, wherein it was suggested that the interaction between PEG and cytochrome-*c* is based on binding to a hydrophobic patch on the surface of the latter.[51] We speculate that such opposing observations are due to PEG's amphiphilicity due to which its behavior depends on the properties of its binding partner.[52]

Since we noticed spatial variations in condensate formation, we surmised that kinetic phenomena play an important role in the PS of Nup98. Consequently, we conducted analysis of the transition of the chemical composition of the Nup98 condensates at different PEG concentrations over time. This examination focuses on the chemical evolution of droplets during the maturation process. We instituted a periodic sampling procedure, wherein BCARS measurements were taken at 5 min and up to a significant span of 24 h post the initiation of PS. The addition of PEG instigates pronounced changes within the Raman spectrum, specifically in the CH stretch region of the droplets (Figures S2 and S3), an effect that displays a monotonic positive relationship with the concentration of PEG (Figure 1D). In the incipient phase of the experiment, especially when a 30% PEG concentration is employed, notable increases in peak intensity at 1000, 2990, and 3065 cm^{-1} were recorded. These are attributed to the glycine residue, the residual asymmetric stretching of the CH_3 groups, and the breathing mode of the aromatic ring of phenylalanine, respectively. This points toward an increase in hydrophobic

https://doi.org/10.1021/acs.biomac.4c00609
Biomacromolecules 2025, 26, 2060−2075

intermolecular interactions among the FG repeating units of the protein chains and suggests possible densification of the protein packing within the droplets.

We also noticed a gradual change in the profile of the amide I peak as the amount of PEG increased: specifically, a decrease in the shoulder at 1645 cm^{-1} over time. To discern the intricacies of the modifications within the secondary structure of Nup98, we performed a spectral deconvolution analysis of the amide I vibration of Nup98 condensates at different PEG concentrations over time (Figures 1E−J and S4). In the absence of a crowding agent, a discernible change in the peak shape and a narrowing over time is observed. Initially, a distinct contribution from the α helix and random coil subpeaks decreases over the course of the experiment and is accompanied by an increase in the contribution from β-sheet and β-turn structures (Figure 1G). In the presence of PEG, this effect is noticeably tempered. Samples containing PEG have a similar amide I peak profile, at early times, to that of the sample that containing no PEG after 24 h of the maturation, albeit with a slightly higher and still rising β-turn content (Figure 1J). These observations indicate that changes in the secondary structure of Nup98 in condensates occur via β-sheet formation and that the "kinetics" (or time-dependence) of this structural maturation process can be expedited through the introduction of PEG. As an alternative method, we quantified thioflavin T (ThT) fluorescence intensity, a molecule that generally indicates β-sheet presence for Nup98 in both 0% PEG and 30% PEG over 24 h. The ThT signal was larger in 30% PEG as compared to 0% PEG at time zero, and both increase over time (Figure S5). While the ∼2-fold increase in ThT fluorescence for both the 0% and 30% PEG/Nup98 droplets does not quantitatively match the increase in β-sheets measured from CARS, the trends are nevertheless the same, showing that the β-sheet content increases during Nup98 droplet aging.

The secondary structure of proteins plays a critical role in defining the mechanical properties of protein droplets. The specific folding patterns, such as β-sheets, dictate the physical strength and elasticity of the droplets, thus influencing their stability and resistance to external stresses.[53−55] Additionally, transformations in these structures can lead to alterations in intermolecular interactions that subsequently impact the viscoelasticity of the droplets. Therefore, an understanding of these structural dynamics is fundamental to comprehending the physical behavior of protein droplets under various conditions. To study how the presence of PEG influences the mechanical properties of the droplets during maturation, we performed FRAP over 5 min to 24 h, in the presence of PEG at varying concentrations. We observed a significant number of amalgamated droplets forming larger spherical condensates during the early stages of the experiment (Figure S6). However, this tendency was subdued with increasing PEG concentrations, resulting in droplets of considerably smaller diameters and more irregular shapes (Figure 2A). For our FRAP studies, we matched the same sampling intervals as those for BCARS.

Intriguingly, even low mean PEG concentrations (2.5% and 5%) resulted in a noticeable slowing of the fluorescence recovery kinetics, even at 5 min after condensate formation. This deceleration was even stronger by the addition of 10% and 30% PEG (Figure 2B). In the overall analysis, the maturation process prominently exhibited a substantial decline in the mobile fraction (Figure 2C), indicating a reduction in the number of freely diffusing particles within the droplets. This phenomenon simultaneously showed a noticeable increase in the half-time recovery (Figure 2D), indicating an extended period required for particle diffusion, as observed from the FRAP experiments. These findings were consistent across all explored concentrations of the crowding agent, suggesting a marked influence on the droplet's internal dynamics and stability. Dynamics of mobile fraction and half-time recovery changes did not exhibit linear time dependence. Rather, they manifested logarithmic decay and growth, respectively. Increasing the PEG concentration correspondingly amplified the slowing mobility trends, resulting in diminished mobile fractions and protracted half-time recoveries in almost all measured cases. The only exception was a slight increase in the mobile fraction for prolonged maturation times in the presence of lower PEG amounts (2.5% and 5%). We additionally performed full droplet bleaching for the 0% and 30% PEG concentrations and found a similar slowing of recovery with time, indicating reduced dynamic exchange of the protein in the droplet phase with that in the continuous phase (Figure S7). Taken together, the structural and physical maturation of Nup98 in the presence of PEG clearly shows that maturation is accelerated at the molecular level. Our data are fully consistent with the increase in the binodal protein concentration with PEG content, according to a fully segregative PS, i.e., concentrating Nup98 and thereby enhancing protein−protein interactions, which correlates with an increase in β-sheet formation. This, in turn, reduces the liquid-like properties of the condensates, as observed through FRAP. While we do not use FRAP to directly prove β-sheet formation, the correlation between increased β-sheet content detected by CARS and the decreased fluidity observed in FRAP is consistent with established findings.[56] The observations herein align with the hypothesis positing that even minimal intermolecular homotypic interactions may be sufficient to establish a percolation pathway. This pathway, in turn, could induce the emergence of dynamically arrested states, culminating in the genesis of gel structures which transform primarily liquid droplets into gel-like aggregates.[57,58]

PEG Crowding Drives Segregative BSA Condensation and Accelerates Physical Maturation. In this section, we study the PS and possible maturation of a solution containing PEG and BSA. BSA is commonly termed a protein with a well-defined, stable, tertiary structure. This makes it an ideal candidate for a comparison with the behavior of disordered Nup98 in terms of how PEG crowding affects condensation and maturation in the case of an ordered protein. BSA primarily consists of alpha-helices, which account for up to 67% of its total secondary structure composition,[59,60] resulting in a consistent and reliable Raman signature that serves as a helpful benchmark for spectroscopic analysis. The robustness and temporal stability of BSA, despite fluctuations in environmental factors, underscore its utility in these investigations.

To study PS and to discern the impact of PEG on the kinetics of BSA condensate maturation, we used the same protocol as that for Nup98. Identical measurement intervals and research techniques were employed, although the PEG concentrations differed. Notably, we observed that BSA does not undergo PS if the concentration of PEG is less than ∼10% (w/v) for solutions with an average BSA concentration of 10 μM (Figure S8). This behavior aligns with findings reported by Poudyal et al. on 8000 g/mol PEG.[38] We note that BSA alone (in excess of 1 mM) or PEG alone (even at 40% (w/v)) formed any droplets. Condensation required BSA and PEG. Furthermore, the noteworthy heterogeneity of the samples warrants mentioning. Unlike Nup98 condensates, BSA droplets were primarily located

https://doi.org/10.1021/acs.biomac.4c00609
Biomacromolecules 2025, 26, 2060−2075

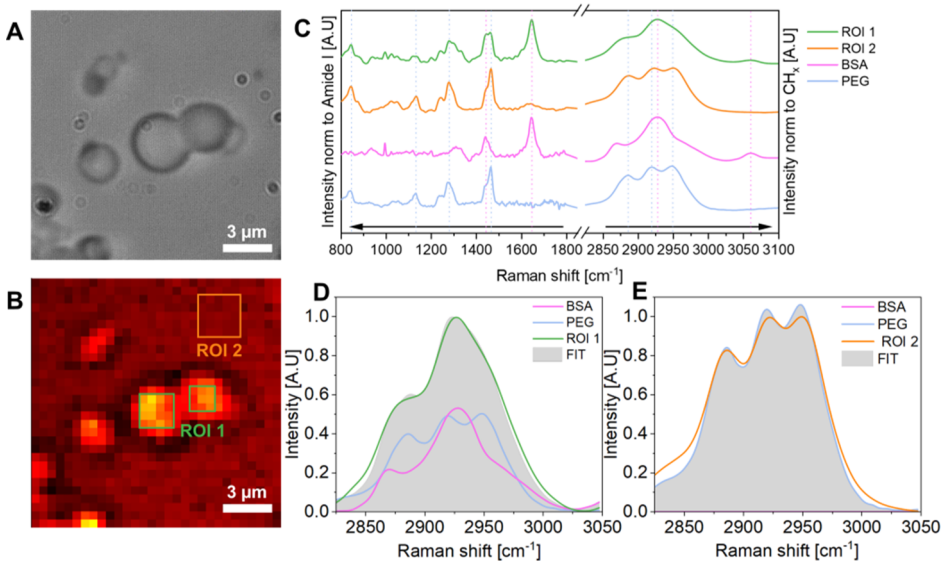

Figure 3. Molecular microscopy of BSA/PEG condensate aging. In situ (A) BF image and (B) BCARS map imaging of the same BSA condensates formed by mixing 1:10 BSA 0.125 mM with PEG 4 kDa 75 mM (30% m/v). Both images were captured 24 h after initiation of LLPS. BCARS map shows averaged CH stretch intensity and is integrated over 2820−3020 cm^{-1} with a pixel size of 0.5 × 0.5 μm. On the BCARS map, ROI 1 marked green, represents a selected part of the droplet phase, and ROI 2 marked orange, represents a selected part of the continuous phase of a sample. (C) Normalized fingerprint and CH stretch spectra comparison of ROI 1 and ROI 2 to 4 mM BSA and 75 mM PEG reference samples. (D) ROI 1 and (E) ROI 2 CH stretch spectral fitting based on BSA and PEG reference samples. Fit is a gray area, and it is a linear sum of BSA and PEG contributions.

Table 1. Summary of BSA and PEG Concentrations for Different Systems[a]

PEG content	component	before mixing [mg·mL^{-1}]	theoretical dilution [mg·mL^{-1}]	droplet phase* [mg·mL^{-1}]	continuous phase* [mg·mL^{-1}]	expected continuous phase [mg·mL^{-1}]
10% PEG	PEG	100	90.90	51.72	91.26	91.47
	BSA	8.25	0.75	53.59	N.A	0
20% PEG	PEG	200	181.82	88.17	167.92	182.66
	BSA	8.25	0.75	83.95	N.A	0
30% PEG	PEG	300	272.73	108.90	247.82	273.56
	BSA	8.25	0.75	148.30	N.A	0

[a]*Indicates directly calculated from BCARS spectra based on mixing 1 μL of BSA and 10 μL of PEG solution.

in the region where the protein solution had been deposited on the coverslip, which hints at a significant diffusion limitation in the mixing of protein with the PEG-containing buffer (Figure S8).

As for Nup98, we analyzed regions of the sample by selecting the locations where both the continuous and droplet phases were clearly observed (Figure 3A). BCARS imaging was initiated in these regions, and we randomly selected a representative number of pixels epitomizing the continuous and droplet phases for spectral analysis (Figure 3B). The acquired spectra from these areas were compared with the spectra of solutions of pure BSA and PEG (Figure 3C). The continuous phase exhibited a Raman-like spectrum almost identical to that of the PEG solution, with common characteristic peaks in both the fingerprint and CH stretch regions. The droplet phase provides more intriguing insights. The fingerprint region contains peaks from both reference spectra, particularly apparent in the peak at 1280 cm^{-1} and the double peak at ∼1455 cm^{-1}. The upper part can be attributed to PEG, whereas the lower one (closer to 1440 cm^{-1}) is associated with BSA, related to various deformations of the CH_2 groups.[45] This shows that the BSA-rich droplets contain a significant fraction of PEG and that the spectrum of the droplet phase in the CH stretch region assumes a unique shape that does not replicate either of the reference spectra.

As mentioned above, the droplet phase comprises both PEG and BSA (Figure 3D). Conversely, the continuous phase is almost devoid of protein (Figure 3E). By deconvoluting the CARS spectra, we quantified the concentrations of BSA and PEG in both phases (Table 1) using spectral fitting. It is evident that the concentration of PEG in the droplet phase is significant, with its value nonlinearly increasing with the mean PEG concentration but never exceeding it. On the other hand, BSA is concentrated in the droplets by 70−190 times the mean value, depending on the mean PEG concentration. The BSA concentration in the continuous phase is below the detection limit and displays a dominance of the crowding agent. In other words, the PS of BSA/PEG/buffer is segregative as well, though not as pronounced as for Nup98/PEG/buffer. Since the mean BSA concentration is very low (see Table 1), the total volume of the dispersed phase is much smaller than that of the continuous phase, implying that the PEG concentration in the continuous phase should be close to the mean or "theoretical" value. Table 1 demonstrates that our spectral quantification method supports this idea. We determined the "expected" PEG concentration in the continuous phase using mass conservation, ensuring that the total amount of PEG remains constant within the system, even as it partitions between phases. Table S1 in the Supporting Information shows how we calculated the expected PEG

https://doi.org/10.1021/acs.biomac.4c00609
Biomacromolecules 2025, 26, 2060−2075

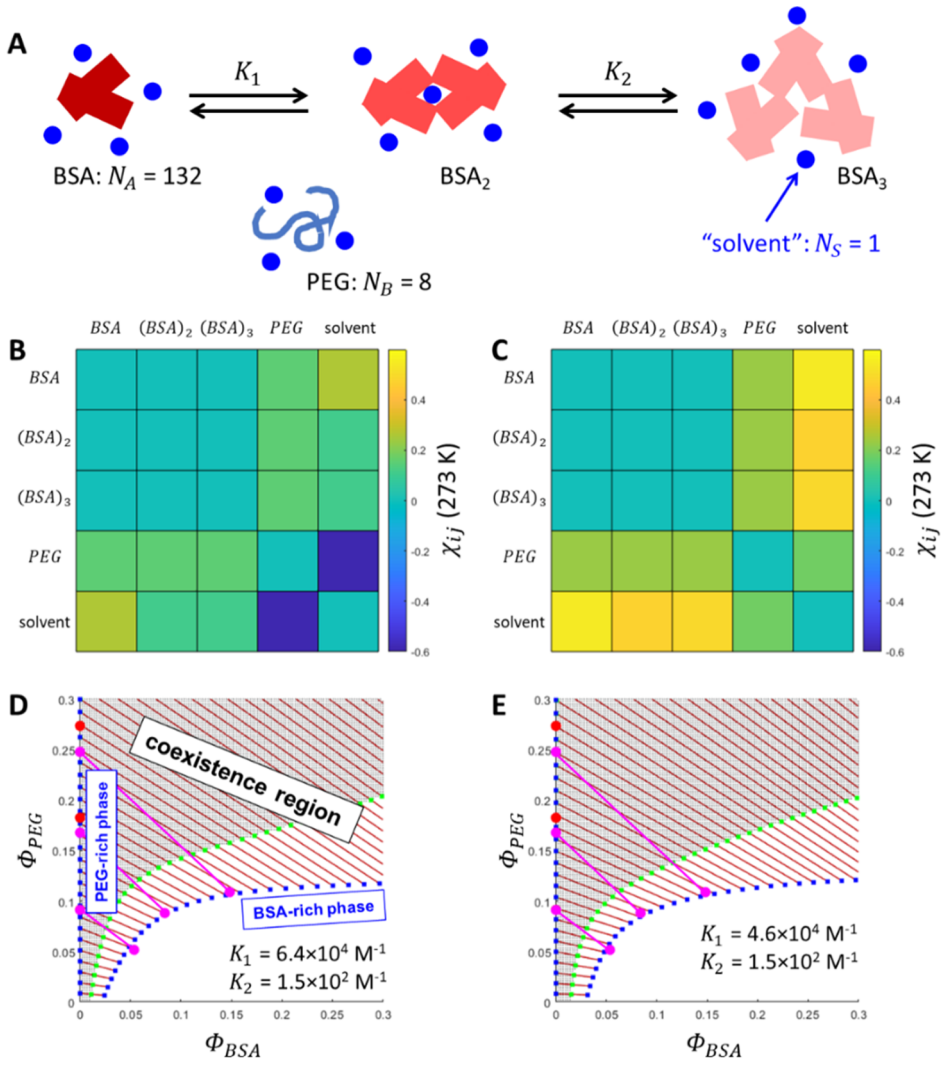

Figure 4. Mean-field modeling predicts BSA/PEG partially segregative PS. (A) Schematic overview of the individual species presumed present in the binary solution BSA/PEG/solvent, together with association constants and relative molecular sizes. (B,C) Matrices containing the sets of best fit values of the binary interaction parameters (χ) at T = 273 K for two scenarios in which we, respectively, assume a good versus a marginal solubility of the BSA in the solvent. For the good solvent scenario (B), we use $0.1 < \chi_{A_{i=1,2,3}S} < 0.3$, whereas for the bad solvent scenario (C), we use $0.45 < \chi_{A_iS} < 0.55$. With these constraints we obtain the values for the BSA-PEG and the PEG-solvent interaction parameters through fitting the model to the experimental data (see panels D,E). (D,E) Experimental and fitted (calculated) phase diagrams, respectively, corresponding to the sets of interaction parameters expressed by panels (B,C) and given association constants. The magenta and red dots on the protein-devoid binodal branch represent measured and expected data, calculated based on mass conservation, assuming the concentrations in the protein-rich phase to be correct. The blue and green squares represent the calculated binodal and spinodal curves, respectively; the magenta (experimental) and brown (calculated) lines are the tie-lines that connect compositions in coexisting phases.

concentration in the continuous phase (Supporting Information, model development).

The fact that the PEG concentration in the dispersed BSA-rich phase gradually increases with the mean value provides the opportunity to obtain more quantitative concentration information from the CARS measurements displayed in Figure 3 by linear unmixing, which is shown in Table 1. Many interactions determine the phase behavior of the BSA/PEG/buffer mixture, and we use the determined concentrations of the binodal together with a free energy model based on mixing theory to interpret different contributing interactions.

Unfortunately, mixing theory in its most basic form, i.e., Flory–Huggins theory,[61] is insufficient to do so, as it does not capture the well-known fact that BSA self-associates into binary and sometimes higher order complexes,[62] which cannot be neglected when calculating the phase diagram of any solution containing this protein. Hence, we present an extended model that combines Flory–Huggins theory with statistical associating fluid theory (SAFT).[63] This type of hybrid model has shown to be an excellent choice for interpreting and predicting biomolecular phase behavior[11,50,64] as it discriminates between nonspecific interactions, captured in a general way by the term "solvation", and specific association between BSA monomers. Unlike scaled particle theory, which has also been used to study effects of crowding on the behavior of (self-)associating proteins,[65] our model includes the solvation of all species, but it disregards contributions relating to the shape of the protein assemblies.

We consider the solution of BSA, PEG, and buffer as a ternary mixture, of which the species are respectively referred to as components A–S (the latter standing for "solvent"). The model considers the propensity of BSA to noncovalently dimerize[66]

https://doi.org/10.1021/acs.biomac.4c00609
Biomacromolecules 2025, 26, 2060–2075

and to some extent form higher order complexes,[62] though without considering the exact mode of association. For this, we define the following binding equilibrium (Figure 4A).

$$A + A \rightleftarrows A_2 \tag{1}$$

$$A_2 + A \rightleftarrows A_3 \tag{2}$$

Characterized by the association constants

$$K_1 = \frac{[A_2]}{[A]^2} \tag{3}$$

$$K_2 = \frac{[A_3]}{[A_2][A]} \tag{4}$$

where the square brackets denote molar concentrations. In other words, due to the BSA self-assembly, we should consider the ternary blend of BSA/PEG/buffer as a quinary mixture, since thermodynamically the BSA complexes should be regarded as additional components. The dimensionless free energy density of this mixture comprises three contributions: one from translational entropy, one from nonspecific interaction, and one from noncovalent binding

$$f \equiv \frac{F}{Nk_BT} = f_{trans} + f_{int} + f_{bind} \tag{5}$$

Here, F is the total free energy, k_BT the thermal energy, and N the total number of sites of an imaginary molecular lattice, onto which we map the mixture.[61] The first and second terms on the RHS of eq 5 are given according to Flory−Huggins theory

$$f_{trans} = \frac{1}{N_A}\left(\phi_A \ln \phi_A + \frac{1}{2}\phi_{A_2} \ln \phi_{A_2} + \frac{1}{3}\phi_{A_3} \ln \phi_{A_3}\right) + \frac{\Phi_B}{N_B} \ln \Phi_B + \Phi_S \ln \Phi_S \tag{6}$$

$$f_{int} = \chi_{A,A_2}\phi_A\phi_{A_2} + \chi_{A,A_3}\phi_A\phi_{A_3} + \chi_{AB}\phi_A\Phi_B + \chi_{AS}\phi_A\Phi_S + \chi_{A_2A_3}\phi_{A_2}\phi_{A_3} + \chi_{A_2B}\phi_{A_2}\Phi_B + \chi_{A_2S}\phi_{A_2}\Phi_S + \chi_{A_3B}\phi_{A_3}\Phi_B + \chi_{A_3S}\phi_{A_3}\Phi_S + \chi_{BS}\Phi_B\Phi_S \tag{7}$$

Here, ϕ_A, ϕ_{A2}, and ϕ_{A_3} are the equilibrium volume fractions of BSA monomers, dimers, and trimers, with the total BSA volume fraction given by $\Phi_A = \phi_A + \phi_{A_2} + \phi_{A_3}$. The parameters N_i denote the effective molecular sizes in terms of lattice sites, Φ_B and $\Phi_S = 1 - \Phi_A - \Phi_B$ are the volume fractions of PEG and solvent and χ_{ij} are Flory parameters. The contribution due to the self-association of BSA is given by

$$f_{bind} = \frac{\Phi_A}{N_A}\left[\frac{1}{2}(p_1 - p_1^\circ) + \frac{2}{3}(p_2 - p_2^\circ) + \ln\left(\frac{1 - p_1 - p_2}{1 - p_1^\circ - p_2^\circ}\right)\right] \tag{8}$$

with p_1 and p_2 the fractions of BSA accommodated in dimers and trimers. The superscript $^\circ$ refers to the pure state. The magnitude of p_1 and p_2 follows from the equilibrium condition $\frac{\partial F}{\partial p_1} = \frac{\partial F}{\partial p_2} = 0$ and the condition that the molecular volume ratio of monomer to dimer to trimer is ∼1/2/3. These constraints give rise to the following conditions

$$2K_1[A]_0 = \frac{p_1}{(1 - p_1 - p_2)^2} \tag{9}$$

$$3K_1K_2[A]_0^2 = \frac{p_2}{(1 - p_1 - p_2)^3} \tag{10}$$

Here, $[A]_0$ is the total molar concentration of BSA. We refer to the Supporting Information (model development) for the derivation of eqs 8, 9, and 10.

We fitted our model against the experimental data (Figure 4), based on two different solubility scenarios, which we detail below. The resulting phase diagrams in panels D and E have been calculated for effective sizes N_i and association constants K_1 and K_2 as specified, as well as the Flory interaction parameter matrices (χ_{ij}), given in panels B and C, respectively. Note that the elements of the latter are given at a reference temperature of T = 273 K, whereas in the calculation we used 300 K, so χ_{ij}(300 K) = χ_{ij}(273 K) × 273/300. The binodal (blue squares), i.e., the actual fit, was calculated by equalizing the chemical potentials and osmotic pressure in the coexisting phases, whereas the spinodal was obtained by the condition det(H) = 0, with H being the Hessian matrix of second derivatives of the free energy with respect to composition. Fitting was subject to seven constraints to limit the number of free-floating variables and eliminate nonuniqueness. In Table 2 we list these constraints, together with a short motivation. Note that constraints 4, 5, and 6 reduce the number of relevant Flory parameters from ten to four.

Table 2. Constraints for Fitting the BSA/PEG/buffer Phase Diagram

entry	constraint	remark
1	$N_S = 1$	the effective molecular size of the "solvent" represents a fundamental volume forming the basis for the normalization of the polymer sizes
2	$K_1 \gg K_2$	the propensity of BSA to form dimers is significantly stronger than to form higher order complexes
3	$\frac{N_A}{N_B} = 16.5$	$\frac{N_A}{N_B}$ reflects (by approximation) the molecular weight ratio of BSA and PEG
4	$\chi_{A,A_2} = \chi_{A,A_3} = \chi_{A_2A_3} = 0$	negligible nonspecific interaction between free and complexed BSA due to chemical similarity
5	$\chi_{AB} = \chi_{A_2B} = \chi_{A_3B} > 0$	interaction of PEG with free and complexed BSA is identical and (effectively) slightly repulsive
6	$0 < \chi_{AS} \approx \chi_{A_2S} = \chi_{A_3S} < 0.55$	the buffer is a good to marginal solvent for BSA and similar for the free and complexed states
7	$\chi_{BS} \ll \frac{1}{2}\left(1 + \frac{1}{\sqrt{N_B}}\right)^2$	the buffer is a very good solvent for PEG: χ_{BS} is significantly lower than its critical value

The two fitting scenarios, respectively, represent the assumption of a good versus marginal solubility of BSA in the buffer, i.e., for the first scenario we have $0.1 < \chi_{A_{i=1,2,3}S} < 0.3$, whereas for the second scenario we take $0.45 < \chi_{A_iS} < 0.55$ (see Figure 4B,C). Note that even for the latter scenario the values for χ_{A_iS} are still too low to cause PS without PEG, in line with the experimental observation. Interestingly, χ_{AS} consistently exceeds χ_{A_2S} and χ_{A_3S}, implying the BSA complexes to be slightly better solvated than unbound BSA. Apart from a small discrepancy in the tie-line angle (which is smallest in the first), we obtain an excellent fit with the experimental results for both scenarios,

https://doi.org/10.1021/acs.biomac.4c00609
Biomacromolecules 2025, 26, 2060−2075

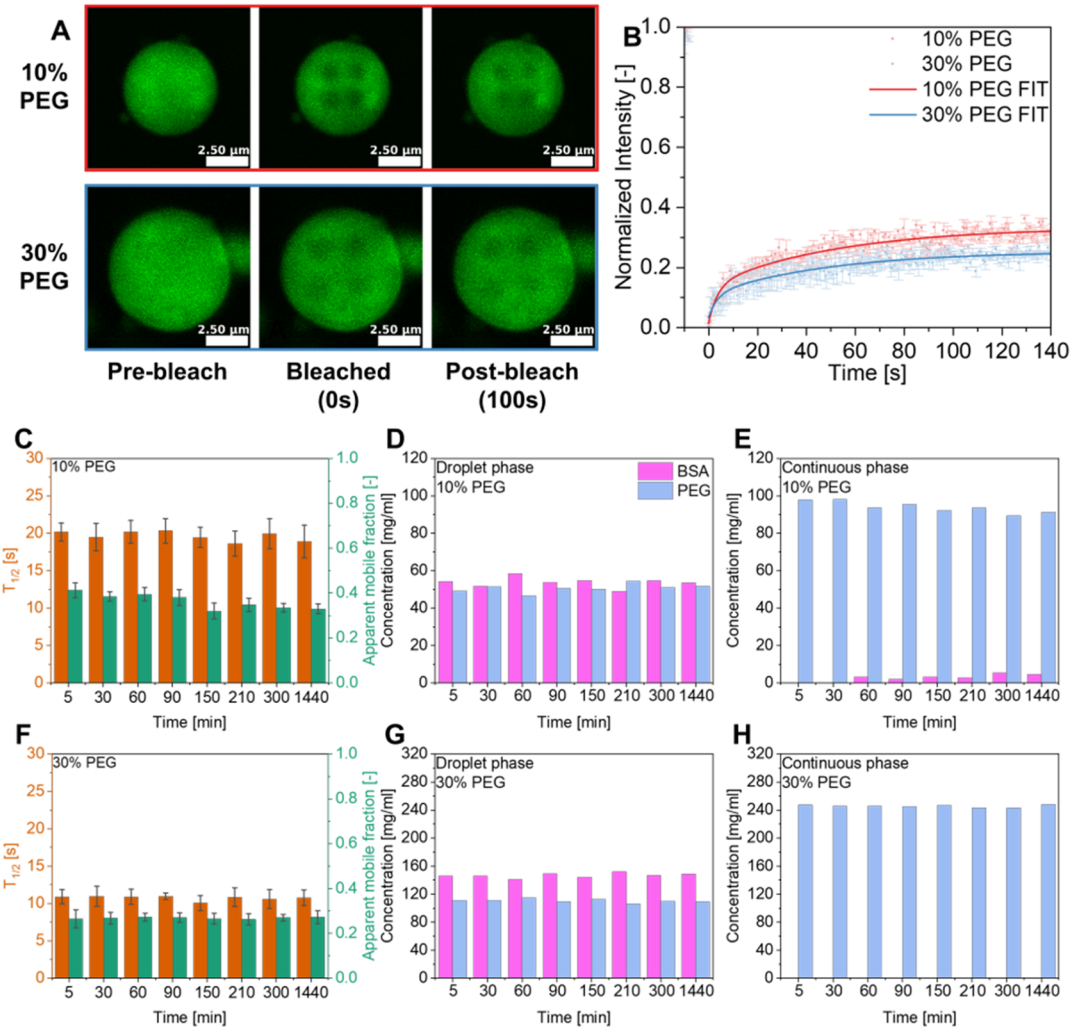

Figure 5. FRAP and concentration analysis of BSA/PEG condensate aging. (A) Representative images from FRAP experiments of 1% FITC-labeled BSA 0.125 mM condensates for 10% PEG and 30% PEG systems captured 5−30 min after initializing LLPS. Each sample was bleached simultaneously in four circular spots with the same diameter of 0.8 μm (10% PEG) and 1.0 μm (30% PEG). (B) Normalized fluorescence intensity of 10% PEG and 30% PEG systems over time after bleaching. The presented curves apply to 24 h maturated samples. Thick lines are fit curves, circular points indicate the average values of 4 bleached regions, and error bars show the standard deviation. Bar graphs of half-time fluorescence recovery and apparent mobility fraction for (C) 10% PEG and (F) 30% PEG systems for different maturation times. Error bars are standard deviations. Concentrations of BSA and PEG over time in the droplet phase for (D) 10% PEG and (G) 30% PEG and continuous phase for (E) 10% PEG, and (H) 30% PEG systems.

reproducing the partially segregative PS and confirming the presence of a significant fraction of PEG in the BSA-rich phase. The fit reveals a mildly repulsive interaction between the BSA and the PEG of χ_{A_iB} = 0.15 and χ_{A_iB} = 0.23 for the first and second scenarios, respectively, as well as a BSA dimerization constant K_1 in the range 10^4−10^5 M^{-1}, which is in good agreement with prior literature.[66] The low trimerization constant K_2 shows that dimerization dominates the formation of higher order BSA complexes, in agreement with the prior observation that near-room-temperature aggregation of BSA is negligible.[62]

The fact that in both scenarios χ_{BS} is low, even negative in the first scenario, is consistent with the notion that low-molecular-weight PEG is very hygroscopic and even deliquescent.[13−15] This result demonstrates that the "crowding action" of this low-molecular-weight PEG mainly stems from its osmolytic nature. We corroborated this by performing additional calculations assuming the crowder to be less soluble (increased χ_{BS}), which shrinks the miscibility gap (see Supporting Information, Figure S9). Although PEG is indeed known to be very hydrophilic, a negative χ_{BS} is less consistent with the literature. Therefore, we deem the second scenario, i.e., assuming a marginal solubility of BSA, to be somewhat more realistic. Finally, the fact that others[38] have observed a more BSA-pure droplet phase in case of a twice longer PEG crowder (8000 kg/mol) is not surprising, given the lowering in translational entropy of a polymer mixture upon increasing the chain length. We corroborated this by performing an additional calculation based on the same input as for Figure 4E but using a twice as large N_B (see Supporting Information, Figure S10). Clearly, the miscibility gap expands and the crowder depletes from the BSA-rich phase, which becomes purer. Our calculations and fitting show that a "minimal model"-based mean-field theory can already profoundly explain how molecular interactions determine the phase behavior of protein/crowder solutions. As we showed in previous work,[11] the key to achieving insight using such minimal models is the categorization of the fundamental interactions present in biomolecular systems in "specific" (associating

https://doi.org/10.1021/acs.biomac.4c00609
Biomacromolecules 2025, 26, 2060−2075

stickers giving defined complexes) and nonspecific (such as solvation).

A notable observation is that in the solutions containing 10% and 30% PEG, the amide I peak remains largely unchanged throughout the 24 h experiment, with major contributions from alpha helices and random coils. This observation is consistent with the well-structured BSA, which maintains an α-helical dominance (Figures S11−S13) for 30% PEG. However, in the 10% PEG sample, we discern a progressive alteration in the ratio of random coils to α helix over time (Figures S11−S13)—helices decrease ∼10% while random coils increase by ∼10%. Similarly, a subtle change in the spectral shape can also be seen for the CH stretch region for 10% PEG in the emergence of a shoulder at 2950 cm^{-1}, which might suggest a slow change in the PEG/BSA ratio inside condensates (Figures S11 and S12). In the case of 30% PEG, neither significant changes in amide I nor CH stretch regions are observed during the 24 h experiment. This behavior elucidates that in the frame of maturation within the BSA-PEG system, any slight alterations in the secondary structure, particularly as witnessed in the 10% PEG system, are not a predominant effect of maturation. Specifically, variations within the secondary structures, such as those within the α helix, may likely be attributed to mere fluctuations, especially in instances where the protein is not sufficiently crowded, as within the 10% PEG condition. Furthermore, higher concentrations of PEG confer stability to the system, enhancing this cooperative dynamic and ensuring that the process is not significantly influenced by minor perturbations in the protein structure but is rather governed by the synergistic participation of both PEG and BSA in the droplet phase.

The composition of biomolecular condensates can profoundly impact their mechanical properties, which are crucial factors in many biological processes. In vitro, the presence of a crowding agent inside the droplets can modulate their dynamics.[67,68] When a crowding agent permeates the droplet, it can influence the viscosity and elasticity of the droplet, hence affecting its physical behavior.[69−71] In addition, the molecules of the crowding agent can contribute to a decrease in the diffusivity of proteins within the droplet. This transition can also influence the interactions between the droplets and their environment. Consequently, comprehending how the presence of crowding agents modulates attributes such as liquidity and viscosity within the droplets provides vital insights into the inherent characteristics and functionalities of these microscopic entities.

To explore changes in droplets' mechanical properties and protein chains' diffusibility inside condensates, with a particular emphasis on the dynamic properties studied over time as a function of PEG content, we used FRAP (Figure 5A). In accordance with the established protocol, the time intervals for these measurements were maintained identical with those for Nup98-based systems. However, in contrast to the Nup98 systems, it was not possible to fully deplete the intensity of the bleached regions in the droplets to near-zero levels. This observation suggests that the recovery of the system might occur on a time scale shorter than our frame capture rate, indicating that the recovery kinetics we are measuring could be an overestimation, particularly in terms of the mobile fraction. Hence, for this system we refer to this measure as the "apparent mobile fraction".

From the beginning of the experiment, both 10% and 30% PEG concentrations exhibit analogous kinetics in the fluorescence recovery process, as evidenced by the similar shapes of their fluorescence recovery curves (Figure 5B). Moreover, we noticed a consistent stability of both the apparent mobile fraction and the half-time of recovery throughout the duration of the 24 h experiment (Figure 5C,F) for both PEG concentrations. FRAP of entire BSA droplets showed almost no recovery, demonstrating the inability for BSA molecular exchange between the droplet and continuous phases. As with partial droplet FRAP, the dynamics in full droplet FRAP were virtually unchanged over 24 h (Figure S14). However, when the PEG concentration was at 10%, we identified marginally more pronounced fluctuations in the half-time of recovery and apparent mobility fraction values. These observations are qualitatively consistent with the Raman data collected on droplet composition for the 10% PEG system, where subtle changes in the amide I and CH stretch spectral regions were also observed in the experiment (Figure 5D). Interestingly, a noticeable rise in the BSA concentration was observed in the continuous phase for 10% PEG, where the initial concentration was below the detection limit at the beginning of the experiment. After approximately 60 min, the concentration rose significantly and exceeded the theoretical mixing concentration (Figure 5E). This prompts us to consider that a 10% PEG concentration may not be adequately sufficient to thoroughly crowd BSA. Modeling intimates that a reduction in crowding agent concentration could steer results toward approaching a possible critical point where both metastable and stable separation regions are separated by slight fraction values. Consequently, minor variations in local concentrations might be the driving force for all observed fluctuations in both Raman and FRAP studies. We note that the apparent absence of BSA in the continuous phase is specifically observed at the 5 and 30 min time points, during which the droplets are still in the process of developing their shape and size. These early stages of droplet formation are characterized by fluctuations in the CARS spectra, which can lead to inconsistencies in the observed mass balance. However, when considering cases where the PEG concentration was 30%, we did not observe a similar change in protein or PEG concentration in either phase (Figure 5G,H). Conversely, at a PEG concentration of 30%, the PS process appears to be spontaneous and a well-defined demixed state is preferable.

DISCUSSION

In this work, we aimed to unravel the intricacies of how PEG interacts with protein droplets, discovering that its influence is multifaceted and varies depending on the particular protein in question. A major observation is that the aging process of protein droplets under the influence of PEG is not uniform across different proteins. When examining Nup98, a disordered protein with many FG tandem repeats, we found that PEG considerably accelerates the chemical and structural changes in the protein when it is condensed. The secondary structure of Nup98 exhibits maturation via the formation of β-sheets in droplets, which is accelerated when PEG is present. We postulate this is because PEG facilitates a denser packing of protein molecules inside the droplets, thereby enhancing their protein−protein sequence-specific, sticker-like interactions and effectively speeding up the kinetics of the maturation process. As established by others, these specific interactions are not essential for PS.[38] Yet, when a crowding agent is introduced, it not only increases the significance of these interactions but may also alter the kinetics associated with changes in viscoelastic and aging properties.[72] Our results with PEG and Nup98 also offer robust support for the hypothesis that even limited but specific, intermolecular Nup98-Nup98 interactions boosted by the

https://doi.org/10.1021/acs.biomac.4c00609
Biomacromolecules 2025, 26, 2060−2075

crowder can stimulate the formation of a percolated network of Nup98 chains. The establishment of such a network is understood to be a pivotal step toward the manifestation of dynamically arrested states characterized by their significant loss of molecular mobility. This dynamic arrest, once initiated, appears to be a mechanistic pathway leading to the formation of a gel-like structure and delineates a transition from a liquid-like state to a solid-like behavior, which is a hallmark of gelation phenomena observed in various protein and RNA systems.[57,58]

Despite how PEG accelerates Nup98 droplet aging, PEG exhibits a sufficiently strong net repulsive interaction with Nup98 as evidenced by fully segregative PS; this means that PEG acts as a true depletant in this case. This behavior aligns closely with the concept of an inert crowding agent wherein the agent exerts a passive influence on the protein. The kinetics of maturation vary based on the amount of crowding agent added to the system. Our observations indicate that PS in the ternary mixture tends to expedite the overall reduction of the mixture's free energy in comparison to binary systems. Introducing even a small quantity of PEG leads to more rapid system stabilization and faster maturation compared to no PEG. Conversely, larger PEG concentrations rapidly solidify as evidenced by limited fusion, reduced mobile fraction, and long half-time recovery when compared to similar maturation times for droplets with less or no PEG. This suggests the presence of two distinct time scales: the first for forming sufficient homotypic interactions to induce PS and yield liquid droplets and a second associated with the gradual shift from liquid condensates to gel-like aggregates. Furthermore, the crowding-agent-dense environment may hasten the β-sheet formation, which could facilitate protein aggregation and amyloid formation. Consequently, this could influence the biological processes triggered by protein piling.[73,74]

In the case of BSA, we observe a distinct interaction with the same PEG crowder. BSA, a structured protein, does not phase-separate on its own, even at concentrations exceeding 100 mg/mL. Yet, adding PEG to the mixture (as low as 5%) alters this behavior such that BSA phase separates at mixture concentrations below 1 mg/mL. Unlike Nup98, BSA droplets contained a significant amount of PEG, showing the net interaction between the polymers to be less repulsive than in the case of PEG/Nup98. Prior studies have shown a similar pattern, where a high concentration of crowding agent is present inside the droplet phase for proteins.[12,75] In contrast to Nup98/PEG, we observed for BSA, as expected, no increase in β-sheet but rather a subtle reduction in helical content and increase in random coils in the case of 10% PEG. Moreover, we saw only minimal changes in molecular mobility from FRAP measurements over the 24 h measurement period. Our calculations show that a significant contribution to the segregative PS between PEG and BSA is the hydrophilicity of the PEG: it effectively enhances the driving force for PS by competing for the solvating environment, thereby favoring homotypic interactions between individual BSA molecules. We therefore conclude that (low molecular weight) PEG acts as an osmolyte similar to, for instance, a hygroscopic salt or highly polar molecules, such as trimethylamine N-oxide (TMAO).

Consistent with a nonrepulsive, segregative PS, for the 10% PEG/BSA system we detect a small amount of BSA in the surrounding phase, which increases with time. This is consistent with the proximity or approach to a critical point for which the protein-devoid branch of the binodal moves away from the composition axis. Nevertheless, any changes in droplet chemistry or mechanics are minimal during the entire examination period, and such changes are even smaller for a high PEG concentration. Consequently, our primary observation is rapid separation of the protein from the solution, with a trade of the helical structure for a random coil structure during the 24 h examination period. With 30% PEG, we find no change in secondary structure nor FRAP dynamics over the entire 24 h period. Interestingly the 30% PEG and 10% PEG with BSA are distinct, suggesting that PEG-induced PS of BSA could "trap" the protein as it takes away solvent or delubricates proteins in the phase separate droplet. Indeed, at 30% PEG the secondary structure is constant overtime, and the secondary structure is unable to change over 24 h, while at 10% the protein can dynamically rearrange into a different structure.

Previous work on peptide self-assembly and fibrillation has revealed that fibril formation proceeds through an LLPS-mediated pathway; that is, LLPS is the intermediate toward the peptide fibrillar assembly. This pathway represents a nonclassical multistep self-assembly mechanism that proceeds the formation of supramolecular assemblies through an LLPS-formed metastable liquid precursor.[76−78] Our current work on aging in protein droplets formed via LLPS in the presence of PEG is consistent with this idea, suggesting the nonclassical self-assembly mechanism also applies to protein self-assembly.

Moreover, it is pertinent to highlight that our investigations revealed limited variations in the secondary structure of BSA compared to those documented for its human analogue, human serum albumin (HSA), by Patel et al.[79] Through application of circular dichroism and ThT imaging, Patel et al. demonstrated that HSA condensates undergo maturation over time, which is concomitant with notable modifications in the secondary structure. These observations are predominantly discernible as an increase in β-sheets over multiple days, a period not probed in our study, as our focus was primarily on the initial stages of droplet formation. Nevertheless, we also executed such experiments with ThT imaging over 3 weeks (Figures S15 and S16). Unlike for HSA or that from previous work with BSA,[38] we found no clear evidence for fibril or fiber-like structures in brightfield or in ThT imaging. Additionally, the ThT signal itself only marginally increased in the sample when kept either on a sealed glass coverslip sandwich or in an Eppendorf tube.

Our study also has certain limitations. First, the buffer conditions were carefully selected to optimize the PS for each protein. Nup98 is typically used in acetate-based buffers, such as TB, which provides the right conditions for in vitro and in-cell experiments. On the other hand, BSA, a folded protein with a well-defined structure, is most commonly found in physiological environments similar to blood, where the buffer contains saline with potassium and phosphate, hence the use of PBS. Although buffer conditions influence PS behavior—BSA droplets form in TB but are smaller than in PBS (Figure S17), our focus remains on the role of the crowding agent, PEG, in driving maturation across these different systems and our differential analysis primarily focuses on each protein individually. We note that in our case, no aggregation or droplet formation of PEG alone was seen (Figure S18). Second, we are also aware of the fact that considering only PEG as a crowder may be somewhat limited. Future studies will include other types of crowders to learn if our conclusions are appropriate for all types of crowding agents. Third, our study focused on two particular proteins, i.e., FG Nups and BSA, as representative of disordered and ordered proteins. It would also be intriguing to examine how different proteins respond to crowding agents and explore the underlying

https://doi.org/10.1021/acs.biomac.4c00609
Biomacromolecules 2025, 26, 2060−2075

mechanisms in these systems. For instance, proteins such as Tau, an intrinsically disordered protein, might illustrate the expulsion mechanism via a net repulsive interaction. Enzymes such as aldolase could demonstrate the osmolyte action where the crowder promotes protein−protein interactions without being repulsive. Additionally, proteins with a strong hydrophilic nature, such as RGG, might be candidates to explore the potential for attractive interactions leading to associative PS. Such studies could provide valuable insights into the diversity of protein-crowd interaction and further expand our understanding of the role of crowding in protein PS.

CONCLUSIONS

Our research shows that the use of a suitable crowding agent can trigger PS across diverse protein families, similar to previous work.[38] Nevertheless, the exact mechanism of crowding varies, depending on the properties of the specific protein exposed to the crowding agent. The mechanism of stimulating PS of the protein may occur based on (1) expulsion of the protein from the solution into a dense phase via a net repulsive interaction and (2) an osmolyte action, wherein the crowder competes with the protein for solvation by the aqueous environment and thus promotes protein−protein interaction without being repulsive. A third mechanism, which we do not observe, is a possible attractive interaction between the protein and crowder to induce associative PS. Thus, crowders in protein PS encompass rich behaviors that promote different phenomena from protein aging to droplet formation depending on the specific proteins involved.

Finally, while we chose Nup98 and BSA with PEG crowding as model systems, the results are potentially relevant to understanding protein behavior in biomedical science. BSA is widely used in biochemistry and molecular biology as a low-interaction protein for formulation optimization, making it a valuable model for studying protein behavior in crowded environments or as a host in catalysis.[80] Similarly, Nup98 dysfunction is implicated in diseases such as cancers and neurodegenerative disorders.[81−83] Given the naturally crowded environment of the NPC, understanding Nup98's behavior could provide insights into its role in disease pathogenesis.

ASSOCIATED CONTENT

Supporting Information

The Supporting Information is available free of charge at https://pubs.acs.org/doi/10.1021/acs.biomac.4c00609.

CLSM images of 1% Alexa Fluor 488-labeled Nup98; normalized BCARS fingerprint and CHx spectra comparison for droplet phase of Nup98:PEG system at various PEG concentrations; normalized BCARS fingerprint and CHx spectra comparison for droplet phase of Nup98:PEG system for 30% PEG and 10% PEG; contribution of subpeaks in Amide I deconvoluted spectra of Nup98:PEG condensate systems; contribution of subpeaks in Amide I deconvoluted spectra of BSA:PEG systems; quantitative intensity measurements of the mean ThT fluorescence signal; normalized fluorescence intensity vs time of 0% PEG and 30% PEG:Nup98 droplets after complete droplet bleaching; representative images from FRAP experiments; model development; and summary of measured concentrations of BSA and PEG in the continuous phase (PDF)

AUTHOR INFORMATION

Corresponding Authors

Jasper J. Michels − *Max Planck Institute for Polymer Research Ackermannweg 10, Mainz 55128, Germany;* orcid.org/0000-0003-1591-4449; Email: michels@mpip-mainz.mpg.de

Sapun H. Parekh − *Department of Biomedical Engineering University of Texas at Austin, Austin, Texas 78712, United States; Max Planck Institute for Polymer Research Ackermannweg 10, Mainz 55128, Germany;* orcid.org/0000-0001-8522-1854; Email: sparekh@utexas.edu

Authors

Mateusz Brzezinski − *Department of Biomedical Engineering University of Texas at Austin, Austin, Texas 78712, United States; Max Planck Institute for Polymer Research Ackermannweg 10, Mainz 55128, Germany*

Pablo G. Argudo − *Max Planck Institute for Polymer Research Ackermannweg 10, Mainz 55128, Germany*

Tom Scheidt − *Biocenter, Johannes Gutenberg University Mainz, Mainz 55128, Germany; Institute of Molecular Biology GmbH, Mainz 55128, Germany*

Miao Yu − *Biocenter, Johannes Gutenberg University Mainz, Mainz 55128, Germany; Institute of Molecular Biology GmbH, Mainz 55128, Germany*

Elnaz Hosseini − *Department of Biomedical Engineering University of Texas at Austin, Austin, Texas 78712, United States; Max Planck Institute for Polymer Research Ackermannweg 10, Mainz 55128, Germany*

Anke Kaltbeitzel − *Max Planck Institute for Polymer Research Ackermannweg 10, Mainz 55128, Germany*

Edward A. Lemke − *Biocenter, Johannes Gutenberg University Mainz, Mainz 55128, Germany; Institute of Molecular Biology GmbH, Mainz 55128, Germany;* orcid.org/0000-0002-0634-0503

Complete contact information is available at: https://pubs.acs.org/10.1021/acs.biomac.4c00609

Author Contributions

M.B., J.J.M., and S.H.P. designed and conceived the study. M.B. and P.A.G. performed and analyzed the CARS experiments with support from S.H.P. M.B. performed and analyzed FRAP studies. E.H. performed the ThT aging and imaging experiments. J.J.M. performed the model calculations and analyzed the resulting data. T.S. M.Y., and E.A.L. analytical reagents and protocols. M.B., J.J.M, and S.H.P. wrote the manuscript with comments from all authors.

Notes

The authors declare no competing financial interest.

ACKNOWLEDGMENTS

S.H.P., E.A.L., and J.J.M. acknowledge support from the Deutsche Forschungsgemeinschaft (DFG) SPP 2191 Molecular Mechanism of functional Phase separation (Project Nr: 402723784). S.H.P. acknowledges support from the DFG #PA2526/3-1/2 and Welch Foundation F-2008-20220331 and National Science Foundation (#2146549). J.J.M. acknowledges the DFG #MI2212/1-1/2. P.A. was funded by a Humboldt Research Fellowship for Postdoctoral Researchers M.Y. was funded by the MSCA Individual Fellowship (TFNUP 89410) and a Humboldt Research Fellowship for Postdoctoral Researchers. T.S. was funded by the EMBO Postdoctoral

Fellowship (ALTF 1020-2020). The content is solely the responsibility of the authors and does not necessarily represent the official views of the funding agencies.

REFERENCES

(1) Hyman, A. A.; Weber, C. A.; Jülicher, F. Liquid-Liquid Phase Separation in Biology. *Annu. Rev. Cell Dev. Biol.* **2014**, *30* (1), 39−58.
(2) Banani, S. F.; Lee, H. O.; Hyman, A. A.; Rosen, M. K. Biomolecular Condensates: Organizers of Cellular Biochemistry. *Nat. Rev. Mol. Cell Biol.* **2017**, *18* (5), 285−298.
(3) Ellis, R. J. Macromolecular Crowding: Obvious but Underappreciated. *Trends Biochem. Sci.* **2001**, *26* (10), 597−604.
(4) Minton, A. P. The Influence of Macromolecular Crowding and Macromolecular Confinement on Biochemical Reactions in Physiological Media. *J. Biol. Chem.* **2001**, *276* (14), 10577−10580.
(5) Hata, Y.; Sawada, T.; Serizawa, T. Macromolecular Crowding for Materials-Directed Controlled Self-Assembly. *J. Mater. Chem. B* **2018**, *6* (40), 6344−6359.
(6) Knowles, D. B.; LaCroix, A. S.; Deines, N. F.; Shkel, I.; Record, M. T. Separation of Preferential Interaction and Excluded Volume Effects on DNA Duplex and Hairpin Stability. *Proc. Natl. Acad. Sci. U.S.A.* **2011**, *108* (31), 12699−12704.
(7) Zimmerman, S. B.; Trach, S. O. Estimation of Macromolecule Concentrations and Excluded Volume Effects for the Cytoplasm of Escherichia Coli. *J. Mol. Biol.* **1991**, *222* (3), 599−620.
(8) Phillip, Y.; Harel, M.; Khait, R.; Qin, S.; Zhou, H.-X.; Schreiber, G. Contrasting Factors on the Kinetic Path to Protein Complex Formation Diminish the Effects of Crowding Agents. *Biophys. J.* **2012**, *103* (5), 1011−1019.
(9) Harada, R.; Sugita, Y.; Feig, M. Protein Crowding Affects Hydration Structure and Dynamics. *J. Am. Chem. Soc.* **2012**, *134* (10), 4842−4849.
(10) Crowe, C. D.; Keating, C. D. Liquid−Liquid Phase Separation in Artificial Cells. *Interface Focus* **2018**, *8* (5), 20180032.
(11) Michels, J. J.; Brzezinski, M.; Scheidt, T.; Lemke, E. A.; Parekh, S. H. Role of Solvent Compatibility in the Phase Behavior of Binary Solutions of Weakly Associating Multivalent Polymers. *Biomacromolecules* **2022**, *23* (1), 349−364.
(12) Qian, D.; Welsh, T. J.; Erkamp, N. A.; Qamar, S.; Nixon-Abell, J.; Krainer, G.; George-Hyslop, P. S.; Michaels, T. C. T.; Knowles, T. P. J. Tie-Lines Reveal Interactions Driving Heteromolecular Condensate Formation. *bioRxiv* **2022**, 2022.02.22.481401.
(13) Baird, J. A.; Olayo-Valles, R.; Rinaldi, C.; Taylor, L. S. Effect of Molecular Weight, Temperature, and Additives on the Moisture Sorption Properties of Polyethylene Glycol. *J. Pharm. Sci.* **2010**, *99* (1), 154−168.
(14) Thijs, H. M. L.; Becer, C. R.; Guerrero-Sanchez, C.; Fournier, D.; Hoogenboom, R.; Schubert, U. S. Water Uptake of Hydrophilic Polymers Determined by a Thermal Gravimetric Analyzer with a Controlled Humidity Chamber. *J. Mater. Chem.* **2007**, *17* (46), 4864.
(15) Marsac, P. J.; Romary, D. P.; Shamblin, S. L.; Baird, J. A.; Taylor, L. S. Spontaneous Crystallinity Loss of Drugs in the Disordered Regions of Poly(Ethylene Oxide) in the Presence of Water. *J. Pharm. Sci.* **2008**, *97* (8), 3182−3194.
(16) Bignotti, F.; Baldi, F.; Grassi, M.; Abrami, M.; Spagnoli, G. Hydrophobically-Modified PEG Hydrogels with Controllable Hydrophilic/Hydrophobic Balance. *Polymers* **2021**, *13* (9), 1489.
(17) Shi, L.; Zhang, J.; Zhao, M.; Tang, S.; Cheng, X.; Zhang, W.; Li, W.; Liu, X.; Peng, H.; Wang, Q. Effects of Polyethylene Glycol on the Surface of Nanoparticles for Targeted Drug Delivery. *Nanoscale* **2021**, *13* (24), 10748−10764.
(18) Israelachvili, J. The Different Faces of Poly(Ethylene Glycol). *Proc. Natl. Acad. Sci. U.S.A.* **1997**, *94* (16), 8378−8379.
(19) Sheth, S. R.; Leckband, D. Measurements of Attractive Forces between Proteins and End-Grafted Poly(Ethylene Glycol) Chains. *Proc. Natl. Acad. Sci. U.S.A.* **1997**, *94* (16), 8399−8404.
(20) André, A. A. M.; Spruijt, E. Liquid−Liquid Phase Separation in Crowded Environments. *IJMS* **2020**, *21* (16), 5908.
(21) Patel, A.; Lee, H. O.; Jawerth, L.; Maharana, S.; Jahnel, M.; Hein, M. Y.; Stoynov, S.; Mahamid, J.; Saha, S.; Franzmann, T. M.; Pozniakovski, A.; Poser, I.; Maghelli, N.; Royer, L. A.; Weigert, M.; Myers, E. W.; Grill, S.; Drechsel, D.; Hyman, A. A.; Alberti, S. A Liquid-to-Solid Phase Transition of the ALS Protein FUS Accelerated by Disease Mutation. *Cell* **2015**, *162* (5), 1066−1077.
(22) Lee, C.-C.; Su, Y.-C.; Ko, T.-P.; Lin, L.-L.; Yang, C.-Y.; Chang, S. S.-C.; Roffler, S. R.; Wang, A. H.-J. Structural Basis of Polyethylene Glycol Recognition by Antibody. *J. Biomed Sci.* **2020**, *27* (1), 12.
(23) André, A. A. M.; Yewdall, N. A.; Spruijt, E. Crowding-Induced Phase Separation and Gelling by Co-Condensation of PEG in NPM1-rRNA Condensates. *Biophys. J.* **2023**, *122* (2), 397−407.
(24) Krull, S.; Thyberg, J.; Björkroth, B.; Rackwitz, H.-R.; Cordes, V. C. Nucleoporins as Components of the Nuclear Pore Complex Core Structure and Tpr as the Architectural Element of the Nuclear Basket. *MBoC* **2004**, *15* (9), 4261−4277.
(25) Patel, S. S.; Belmont, B. J.; Sante, J. M.; Rexach, M. F. Natively Unfolded Nucleoporins Gate Protein Diffusion across the Nuclear Pore Complex. *Cell* **2007**, *129* (1), 83−96.
(26) Ader, C.; Frey, S.; Maas, W.; Schmidt, H. B.; Görlich, D.; Baldus, M. Amyloid-like Interactions within Nucleoporin FG Hydrogels. *Proc. Natl. Acad. Sci. U.S.A.* **2010**, *107* (14), 6281−6285.
(27) Danilov, L. G.; Moskalenko, S. E.; Matveenko, A. G.; Sukhanova, X. V.; Belousov, M. V.; Zhouravleva, G. A.; Bondarev, S. A. The Human NUP58 Nucleoporin Can Form Amyloids In Vitro and In Vivo. *Biomedicines* **2021**, *9* (10), 1451.
(28) Frey, S.; Görlich, D. A. Saturated FG-Repeat Hydrogel Can Reproduce the Permeability Properties of Nuclear Pore Complexes. *Cell* **2007**, *130* (3), 512−523.
(29) Lelos, M. Overview of Alzheimer's and Parkinson's Diseases and the Role of Protein Aggregation in These Neurodegenerative Diseases. In *Handbook of Innovations in Central Nervous System Regenerative Medicine*; Elsevier, 2020; pp 29−53..
(30) Salahuddin, P.; Fatima, M. T.; Uversky, V. N.; Khan, R. H.; Islam, Z.; Furkan, M. The Role of Amyloids in Alzheimer's and Parkinson's Diseases. *Int. J. Biol. Macromol.* **2021**, *190*, 44−55.
(31) Lecerf, J.-M.; Shirley, T. L.; Zhu, Q.; Kazantsev, A.; Amersdorfer, P.; Housman, D. E.; Messer, A.; Huston, J. S. Human Single-Chain Fv Intrabodies Counteract in Situ Huntingtin Aggregation in Cellular Models of Huntington's Disease. *Proc. Natl. Acad. Sci. U.S.A.* **2001**, *98* (8), 4764−4769.
(32) Ross, C. A.; Tabrizi, S. J. Huntington's Disease: From Molecular Pathogenesis to Clinical Treatment. *Lancet Neurology* **2011**, *10* (1), 83−98.
(33) Sinsky, J.; Pichlerova, K.; Hanes, J. Tau Protein Interaction Partners and Their Roles in Alzheimer's Disease and Other Tauopathies. *IJMS* **2021**, *22* (17), 9207.
(34) Hoffmann, W.; Folmert, K.; Moschner, J.; Huang, X.; Von Berlepsch, H.; Koksch, B.; Bowers, M. T.; Von Helden, G.; Pagel, K. NFGAIL Amyloid Oligomers: The Onset of Beta-Sheet Formation and the Mechanism for Fibril Formation. *J. Am. Chem. Soc.* **2018**, *140* (1), 244−249.
(35) Buchanan, L. E.; Dunkelberger, E. B.; Tran, H. Q.; Cheng, P.-N.; Chiu, C.-C.; Cao, P.; Raleigh, D. P.; De Pablo, J. J.; Nowick, J. S.; Zanni, M. T. Mechanism of IAPP Amyloid Fibril Formation Involves an Intermediate with a Transient β-Sheet. *Proc. Natl. Acad. Sci. U.S.A.* **2013**, *110* (48), 19285−19290.
(36) Burdine, R. D.; Preston, C. C.; Leonard, R. J.; Bradley, T. A.; Faustino, R. S. Nucleoporins in Cardiovascular Disease. *J. Mol. Cell. Cardiol.* **2020**, *141*, 43−52.
(37) Annunziata, O.; Asherie, N.; Lomakin, A.; Pande, J.; Ogun, O.; Benedek, G. B. Effect of Polyethylene Glycol on the Liquid−Liquid Phase Transition in Aqueous Protein Solutions. *Proc. Natl. Acad. Sci. U.S.A.* **2002**, *99* (22), 14165−14170.
(38) Poudyal, M.; Patel, K.; Gadhe, L.; Sawner, A. S.; Kadu, P.; Datta, D.; Mukherjee, S.; Ray, S.; Navalkar, A.; Maiti, S.; Chatterjee, D.; Devi, J.; Bera, R.; Gahlot, N.; Joseph, J.; Padinhateeri, R.; Maji, S. K. Intermolecular Interactions Underlie Protein/Peptide Phase Separa-

https://doi.org/10.1021/acs.biomac.4c00609
Biomacromolecules 2025, 26, 2060−2075

tion Irrespective of Sequence and Structure at Crowded Milieu. *Nat. Commun.* **2023**, *14* (1), 6199.
(39) Konishi, H. A.; Yoshimura, S. H. Interactions between Non-structured Domains of FG- and non-FG-nucleoporins Coordinate the Ordered Assembly of the Nuclear Pore Complex in Mitosis. *FASEB j.* **2020**, *34* (1), 1532−1545.
(40) Milles, S.; Huy Bui, K.; Koehler, C.; Eltsov, M.; Beck, M.; Lemke, E. A. Facilitated Aggregation of FG Nucleoporins under Molecular Crowding Conditions. *EMBO Rep.* **2013**, *14* (2), 178−183.
(41) Samuel, A. Z.; Umapathy, S. Energy Funneling and Macromolecular Conformational Dynamics: A 2D Raman Correlation Study of PEG Melting. *Polym. J.* **2014**, *46* (6), 330−336.
(42) Kung, M.-L.; Lin, P.-Y.; Hsieh, C.-W.; Hsieh, S. Aqueous Self-Assembly and Surface-Functionalized Nanodots for Live Cell Imaging and Labeling. *Nano Res.* **2014**, *7* (8), 1164−1176.
(43) Šebek, J.; Pele, L.; Potma, E. O.; Benny Gerber, R. Raman Spectra of Long Chain Hydrocarbons: Anharmonic Calculations, Experiment and Implications for Imaging of Biomembranes. *Phys. Chem. Chem. Phys.* **2011**, *13* (28), 12724.
(44) Howell, N. K.; Arteaga, G.; Nakai, S.; Li-Chan, E. C. Y. Raman Spectral Analysis in the C−H Stretching Region of Proteins and Amino Acids for Investigation of Hydrophobic Interactions. *J. Agric. Food Chem.* **1999**, *47* (3), 924−933.
(45) Adar, F. Interpretation of Raman Spectrum of Proteins. *Spectroscopy* **2022**, *9*−*13*, 9.
(46) Sagitova, E. A.; Prokhorov, K. A.; Nikolaeva, G. Y.; Baimova, A. V.; Pashinin, P. P.; Yarysheva, A. Y.; Mendeleev, D. I. Raman Analysis of Polyethylene Glycols and Polyethylene Oxides. *J. Phys.: Conf. Ser.* **2018**, *999*, 012002.
(47) Gontrani, L.; Tagliatesta, P.; Agresti, A.; Pescetelli, S.; Carbone, M. New Insights into the Structure of Glycols and Derivatives: A Comparative X-Ray Diffraction, Raman and Molecular Dynamics Study of Ethane-1,2-Diol, 2-Methoxyethan-1-Ol and 1,2-Dimethoxy Ethane. *Crystals* **2020**, *10* (11), 1011.
(48) Rooney, R. T.; Schmitt, K. G.; Von Horsten, H. F.; Schmidt, R.; Gewirth, A. A. Raman and QCM Studies of PPG and PEG Adsorption on Cu Electrode Surfaces. *J. Electrochem. Soc.* **2018**, *165* (14), D687−D695.
(49) Kuzmin, V. V.; Novikov, V. S.; Ustynyuk, L. Yu.; Prokhorov, K. A.; Sagitova, E. A.; Nikolaeva, G. Yu Raman Spectra of Polyethylene Glycols: Comparative Experimental and DFT Study. *J. Mol. Struct.* **2020**, *1217*, 128331.
(50) Chauhan, G.; Bremer, A.; Dar, F.; Mittag, T.; Pappu, R. V. Crowder Titrations Enable the Quantification of Driving Forces for Macromolecular Phase Separation. *Biophys. J.* **2024**, *123* (11), 1376−1392.
(51) Crowley, P. B.; Brett, K.; Muldoon, J. NMR Spectroscopy Reveals Cytochrome *c* − Poly(Ethylene Glycol) Interactions. *ChemBioChem* **2008**, *9* (5), 685−688.
(52) Parray, Z. A.; Hassan, M. I.; Ahmad, F.; Islam, A. Amphiphilic Nature of Polyethylene Glycols and Their Role in Medical Research. *Polym. Test.* **2020**, *82*, 106316.
(53) Chen, G.; Xu, T.; Yan, Y.; Zhou, Y.; Jiang, Y.; Melcher, K.; Xu, H. E. Amyloid Beta: Structure, Biology and Structure-Based Therapeutic Development. *Acta Pharmacol. Sin.* **2017**, *38* (9), 1205−1235.
(54) Elsawy, M. A.; Smith, A. M.; Hodson, N.; Squires, A.; Miller, A. F.; Saiani, A. Modification of *β*-Sheet Forming Peptide Hydrophobic Face: Effect on Self-Assembly and Gelation. *Langmuir* **2016**, *32* (19), 4917−4923.
(55) Meng, Q.; Wang, K.; Li, H.; Guo, S.; Wei, F.; Qi, J.; Sui, Y.; Zhao, X. Single Crystal Shear Moduli of *β*-Phase Stabilized by Thermo-mechanical Treatment in TiNbSn Alloys with Ultralow Elastic Modulus. *Mater. Lett.* **2021**, *285*, 129103.
(56) Celetti, G.; Paci, G.; Caria, J.; VanDelinder, V.; Bachand, G.; Lemke, E. A. The Liquid State of FG-Nucleoporins Mimics Permeability Barrier Properties of Nuclear Pore Complexes. *J. Cell Biol.* **2020**, *219* (1), No. e201907157.
(57) Erkamp, N. A.; Sneideris, T.; Ausserwöger, H.; Qian, D.; Qamar, S.; Nixon-Abell, J.; St George-Hyslop, P.; Schmit, J. D.; Weitz, D. A.; Knowles, T. P. J. Spatially Non-Uniform Condensates Emerge from Dynamically Arrested Phase Separation. *Nat. Commun.* **2023**, *14* (1), 684.
(58) Wadsworth, G. M.; Zahurancik, W. J.; Zeng, X.; Pullara, P.; Lai, L. B.; Sidharthan, V.; Pappu, R. V.; Gopalan, V.; Banerjee, P. R. RNAs Undergo Phase Transitions with Lower Critical Solution Temperatures. *Nat. Chem.* **2023**, *15* (12), 1693−1704.
(59) Chudzik, M.; Maciążek-Jurczyk, M.; Pawełczak, B.; Sułkowska, A. Spectroscopic Studies on the Molecular Ageing of Serum Albumin. *Molecules* **2017**, *22* (1), 34.
(60) Lu, R.; Li, W.-W.; Katzir, A.; Raichlin, Y.; Yu, H.-Q.; Mizaikoff, B. Probing the Secondary Structure of Bovine Serum Albumin during Heat-Induced Denaturation Using Mid-Infrared Fiberoptic Sensors. *Analyst* **2015**, *140* (3), 765−770.
(61) Wall, F. T., Flory, P. J.. *Principles of Polymer Chemistry*. Cornell Univ. Press, Ithaca, NY, 1953. 688 Pp. Illus. $8.50. Science, 1954, *119* (3095), 555−556. DOI: .
(62) Molodenskiy, D.; Shirshin, E.; Tikhonova, T.; Gruzinov, A.; Peters, G.; Spinozzi, F. Thermally Induced Conformational Changes and Protein−Protein Interactions of Bovine Serum Albumin in Aqueous Solution under Different pH and Ionic Strengths as Revealed by SAXS Measurements. *Phys. Chem. Chem. Phys.* **2017**, *19* (26), 17143−17155.
(63) Economou, I. G. Statistical Associating Fluid Theory: A Successful Model for the Calculation of Thermodynamic and Phase Equilibrium Properties of Complex Fluid Mixtures. *Ind. Eng. Chem. Res.* **2002**, *41* (5), 953−962.
(64) Pappu, R. V.; Cohen, S. R.; Dar, F.; Farag, M.; Kar, M. Phase Transitions of Associative Biomacromolecules. *Chem. Rev.* **2023**, *123* (14), 8945−8987.
(65) Guseman, A. J.; Perez Goncalves, G. M.; Speer, S. L.; Young, G. B.; Pielak, G. J. Protein Shape Modulates Crowding Effects. *Proc. Natl. Acad. Sci. U.S.A.* **2018**, *115* (43), 10965−10970.
(66) Levi, V.; González Flecha, F. L. Reversible Fast-Dimerization of Bovine Serum Albumin Detected by Fluorescence Resonance Energy Transfer. *Biochim. Biophys. Acta, Proteins Proteomics* **2002**, *1599* (1−2), 141−148.
(67) Kuznetsova, I.; Turoverov, K.; Uversky, V. What Macromolecular Crowding Can Do to a Protein. *IJMS* **2014**, *15* (12), 23090−23140.
(68) Mukherjee, S.; Waegele, M. M.; Chowdhury, P.; Guo, L.; Gai, F. Effect of Macromolecular Crowding on Protein Folding Dynamics at the Secondary Structure Level. *J. Mol. Biol.* **2009**, *393* (1), 227−236.
(69) Lecinski, S.; Shepherd, J. W.; Bunting, K.; Dresser, L.; Quinn, S. D.; MacDonald, C.; Leake, M. C. Correlating Viscosity and Molecular Crowding with Fluorescent Nanobeads and Molecular Probes: In Vitro and in Vivo. *Interface Focus* **2022**, *12* (6), 20220042.
(70) Lemetti, L.; Hirvonen, S.-P.; Fedorov, D.; Batys, P.; Sammalkorpi, M.; Tenhu, H.; Linder, M. B.; Aranko, A. S. Molecular Crowding Facilitates Assembly of Spidroin-like Proteins through Phase Separation. *Eur. Polym. J.* **2019**, *112*, 539−546.
(71) Cinar, H.; Oliva, R.; Wu, H.; Zhang, M.; Chan, H. S.; Winter, R. Effects of Cosolvents and Crowding Agents on the Stability and Phase Transition Kinetics of the SynGAP/PSD-95 Condensate Model of Postsynaptic Densities. *J. Phys. Chem. B* **2022**, *126* (8), 1734−1741.
(72) Alshareedah, I.; Borcherds, W.; Cohen, S.; Farag, M.; Singh, A.; Bremer, A.; Pappu, R.; Mittag, T.; Banerjee, P. Sequence-Specific Interactions Determine Viscoelastic Moduli and Aging Dynamics of Protein Condensates. *bioRxiv* June *22*, **2023**. DOI: .
(73) Meisl, G.; Xu, C. K.; Taylor, J. D.; Michaels, T. C. T.; Levin, A.; Otzen, D.; Klenerman, D.; Matthews, S.; Linse, S.; Andreasen, M.; Knowles, T. P. J. Uncovering the Universality of Self-Replication in Protein Aggregation and Its Link to Disease. *Sci. Adv.* **2022**, *8* (32), No. eabn6831.
(74) Meisl, G.; Hidari, E.; Allinson, K.; Rittman, T.; DeVos, S. L.; Sanchez, J. S.; Xu, C. K.; Duff, K. E.; Johnson, K. A.; Rowe, J. B.; Hyman, B. T.; Knowles, T. P. J.; Klenerman, D. In Vivo Rate-Determining Steps of Tau Seed Accumulation in Alzheimer's Disease. *Sci. Adv.* **2021**, *7* (44), No. eabh1448.

https://doi.org/10.1021/acs.biomac.4c00609
Biomacromolecules 2025, 26, 2060−2075

(75) Emmanouilidis, L.; Bartalucci, E.; Kan, Y.; Ijavi, M.; Pérez, M. E.; Afanasyev, P.; Boehringer, D.; Zehnder, J.; Parekh, S. H.; Bonn, M.; Michaels, T. C. T.; Wiegand, T.; Allain, F. H.-T. A Solid Beta-Sheet Structure Is Formed at the Surface of FUS Liquid Droplets during Aging. *bioRxiv* June *3*, **2023**. DOI: .
(76) Yuan, C.; Li, Q.; Xing, R.; Li, J.; Yan, X. Peptide Self-Assembly through Liquid-Liquid Phase Separation. *Chem.* **2023**, *9* (9), 2425−2445.
(77) Yuan, C.; Xing, R.; Cui, J.; Fan, W.; Li, J.; Yan, X. Multistep Desolvation as a Fundamental Principle Governing Peptide Self-Assembly Through Liquid−Liquid Phase Separation. *CCS Chem.* **2024**, *6* (1), 255−265.
(78) Yuan, C.; Levin, A.; Chen, W.; Xing, R.; Zou, Q.; Herling, T. W.; Challa, P. K.; Knowles, T. P. J.; Yan, X. Nucleation and Growth of Amino Acid and Peptide Supramolecular Polymers through Liquid−Liquid Phase Separation. *Angew. Chem. Int. Ed* **2019**, *58* (50), 18116−18123.
(79) Patel, C. K.; Singh, S.; Saini, B.; Mukherjee, T. K. Macromolecular Crowding-Induced Unusual Liquid−Liquid Phase Separation of Human Serum Albumin via Soft Protein−Protein Interactions. *J. Phys. Chem. Lett.* **2022**, *13* (16), 3636−3644.
(80) Testa, A.; Dindo, M.; Rebane, A. A.; Nasouri, B.; Style, R. W.; Golestanian, R.; Dufresne, E. R.; Laurino, P. Sustained Enzymatic Activity and Flow in Crowded Protein Droplets. *Nat. Commun.* **2021**, *12* (1), 6293.
(81) Xu, S.; Powers, M. A. Nuclear Pore Proteins and Cancer. *Semin. Cell Dev. Biol.* **2009**, *20* (5), 620−630.
(82) D'Angelo, M. A.; Hetzer, M. W. Structure, Dynamics and Function of Nuclear Pore Complexes. *Trends Cell Biol.* **2008**, *18* (10), 456−466.
(83) Raices, M.; D'Angelo, M. A. Nuclear Pore Complex Composition: A New Regulator of Tissue-Specific and Developmental Functions. *Nat. Rev. Mol. Cell Biol.* **2012**, *13* (11), 687−699.
(84) Heidari, M.; Hummer, G. Yu_et_al_2023_molecular_dynamics_simulation_data, **2023**. DOI: .
(85) Adam, S. A.; Marr, R. S.; Gerace, L. Nuclear Protein Import in Permeabilized Mammalian Cells Requires Soluble Cytoplasmic Factors. *J. Cell Biol.* **1990**, *111* (3), 807−816.
(86) Koulouras, G.; Panagopoulos, A.; Rapsomaniki, M. A.; Giakoumakis, N. N.; Taraviras, S.; Lygerou, Z. EasyFRAP-Web: A Web-Based Tool for the Analysis of Fluorescence Recovery after Photobleaching Data. *Nucleic Acids Res.* **2018**, *46* (W1), W467−W472.
(87) Rapsomaniki, M. A.; Kotsantis, P.; Symeonidou, I.-E.; Giakoumakis, N.-N.; Taraviras, S.; Lygerou, Z. easyFRAP: An Interactive, Easy-to-Use Tool for Qualitative and Quantitative Analysis of FRAP Data. *Bioinformatics* **2012**, *28* (13), 1800−1801.
(88) Giakoumakis, N. N.; Rapsomaniki, M. A.; Lygerou, Z. Analysis of Protein Kinetics Using Fluorescence Recovery After Photobleaching (FRAP). In *Analysis of Protein Kinetics Using Fluorescence Recovery After Photobleaching (FRAP)*; Microscopy, L., Markaki, Y., Harz, H., Eds.; Springer New York: New York, NY, 2017; Vol. *1563*, pp 243−267..
(89) Billecke, N.; Bosma, M.; Rock, W.; Fleissner, F.; Best, G.; Schrauwen, P.; Kersten, S.; Bonn, M.; Hesselink, M. K. C.; Parekh, S. H. Perilipin 5 Mediated Lipid Droplet Remodelling Revealed by Coherent Raman Imaging. *Integr. Biol.* **2015**, *7* (4), 467−476.
(90) Liu, Y.; Lee, Y. J.; Cicerone, M. T. Broadband CARS Spectral Phase Retrieval Using a Time-Domain Kramers−Kronig Transform. *Opt. Lett.* **2009**, *34* (9), 1363.
(91) Chatterjee, S.; Kan, Y.; Brzezinski, M.; Koynov, K.; Regy, R. M.; Murthy, A. C.; Burke, K. A.; Michels, J. J.; Mittal, J.; Fawzi, N. L.; Parekh, S. H. Reversible Kinetic Trapping of FUS Biomolecular Condensates. *Advanced Science* **2022**, *9* (4), 2104247.

https://doi.org/10.1021/acs.biomac.4c00609
Biomacromolecules 2025, 26, 2060−2075